FACULTY OF MATHEMATICS AND PHYSICS
Charles University

MASTER THESIS

Radka Štefaníková

Heterogeneous metal-plasma polymer nanoparticles prepared by means of gas aggregation sources

Department of Macromolecular Physics

Supervisor of the master thesis: doc. RNDr. Ondřej Kylián, Ph.D.

Study programme: Physics

Study branch: Physics of Condensed Matter and Materials

Prague 2020

I declare that I carried out this master thesis independently, and only with the cited sources, literature and other professional sources. It has not been used to obtain another or the same degree.

I understand that my work relates to the rights and obligations under the Act No. 121/2000 Sb., the Copyright Act, as amended, in particular the fact that the Charles University has the right to conclude a license agreement on the use of this work as a school work pursuant to Section 60 subsection 1 of the Copyright Act.

In . . . . date . . . .
                                                        Author's signature

Title: Heterogeneous metal-plasma polymer nanoparticles prepared by means of gas aggregation sources

Author: Radka Štefaníková

Department: Department of Macromolecular Physics

Supervisor: doc. RNDr. Ondřej Kylián, Ph.D., Department of Macromolecular Physics

Abstract: The field of nanoparticle preparation is nowadays rapidly evolving. Most of the approaches can be classified as wet chemistry techniques. On the other hand, gas aggregation sources offer an alternative, purely physical approach of how to fabricate nanoparticles in a controlled and reproducible manner.

Many kinds of nanoparticles were already produced in this way, e.g. metallic, metal oxides or plasma polymer nanoparticles. Moreover, as it was demonstrated in recent studies, even heterogeneous nanoparticles by combining more types of materials may be produced by such sources. Among them, an increasing interest is devoted to the metal/plasma polymer nanoparticles.

Concerning the production of metal/plasma polymers nanoparticles, the majority of so far published studies focused on the nanoparticles with metallic cores surrounded by a plasma polymer overcoat. Because of this, we decided to investigate a novel two-step deposition procedure for the production of metal/plasma polymer nanoparticles with inverse structure, i.e. nanoparticles with plasma polymer cores covered by metal. This method is based on the gas aggregation technique for plasma polymer nanoparticle fabrication (C:H:N:O in this study) followed by subsequent in-flight coating by sputtered metal (silver, copper and titanium). The production process was monitored in terms of deposition rate, magnetron voltage, optical emission and laser light scattering. Ex situ characterization of produced nanoparticles was done by SEM, TEM, XPS and UV-Vis.

For most of the experiments reported in this thesis, silver was used for coating of plasma polymer nanoparticles. It was shown that nanoparticles with plasma polymer cores decorated with silver satellites were obtained in this case. The silver satellites stemmed from the island growth of Ag on the plasma polymer core particle that was serving as a substrate. Moreover, it was found that the size and number of silver satellites presented on C:H:N:O cores may be controlled by the amount of sputtered silver.

However, preliminary experiments that were performed with copper and titanium revealed that the mechanism of satellite formation might not be generally applicable for other metals.

Keywords: gas aggregation plasma polymer heterogeneous nanoparticles magnetron sputtering

Contents

Introduction

Nanoparticles have been receiving much attention during past few decades, mainly due to their high surface-to-volume ratio. This attribute plays a major role when it comes to their properties (e.g. optical, electrical, magnetic, (photo)catalytic) and leads to many interesting applications in areas such as data storage, drug delivery, sensing or solar cells.

For this reason, many ways of nanoparticle fabrication have been developed, based mainly on wet-chemistry methods. Naturally, this approach might, and often does, incorporate usage of toxic chemicals and not easily controllable many-step processes. Although the latter was mastered to a certain extent to industrial applications, the former still might be avoided.

Historically, parallel to the development of wet-chemistry synthesis, vacuum-based techniques were extensively studied, but used mostly for thin film depositions. An important advance in this field with respect to the nanoparticle preparation was done in 1990 when Haberland and his colleagues reported on a novel cluster source combining gas aggregation with magnetron sputtering. [1] Since then a notable development was achieved improving efficiency and understanding of processes taking place during nanoparticle production and widening the range of materials from which nanoparticles may be produced. There are also many other advantages of such an approach: this technique is solvent free, allows for the production of nanoparticles with high purity, does not contain harsh chemicals and can be therefore considered as an eco-friendly process with promising future industrial applications.

Most of the following early works were mainly focusing on single material nanoparticle preparation [2, 3, 4], while nowadays the interest is moving towards composite, heterogeneous two- or multi-component nanoparticles with an aim to synthesize nanomaterials with novel or enhanced functional properties. [5, 6, 7]

All the previously cited articles were investigating solely metals or oxides, but there is also another class of materials that came into focus – plasma polymers. Plasma polymers constitute a family of macromolecular solids that are created as a result of passage of organic vapours or precursors through plasma. Due to the stochastic way of their formation, plasma polymers do not possess the same structure as conventional polymers: there are no regularly repeated subunits, the structure is quite irregular and the chemical composition can differ from that of used monomers. On the other hand, it is possible to create plasma polymers with properties not achievable with conventional polymers. Furthermore, plasma polymers can be easily functionalized due to high concentration of radicals and unsaturated bonds, and their structure and functionality may be at some extent controlled by the deposition conditions. Such materials are then useful in a wide range of applications, where they are used for instance as dielectric, barrier or protective layers or as coatings that regulate wettability or bioadhesive properties of coated objects.

Although plasma polymers were traditionally deposited in a form of thin films, early works in the sixties of the last century reported that at certain deposition conditions, typically at elevated pressures, the formation of micron and sub-micron size plasma polymer particles occurs in the plasma volume. [8] These

findings paved the way to the production of plasma polymer nanoparticles with tailor-made properties. Concerning this, the Haberland type of gas aggregation source was over the last few years demonstrated to be a suitable tool for controlled deposition of various types of plasma polymer nanoparticles. [9, 10]

Furthermore, recent works conducted at the Department of Macromolecular Physics proved that it is also possible to employ gas aggregation sources for the production of heterogeneous metal/plasma polymer nanoparticles that may be of high interest e.g. for (bio)sensing or for biomedical applications. [11, 12]

The aim of this thesis is further investigation of methods for the fabrication of these metal/plasma polymer nanoparticles. While in the previous studies the metal/plasma polymer nanoparticles had metallic cores and plasma polymer shell, we have decided to reverse the structure of produced nanoparticles in this study, i.e. to produce plasma polymer core that is covered by a metallic layer.

For this purpose, the thesis is divided into three chapters followed by a conclusion, in which the major outcomes are summed up. In the first chapter, the theoretical background of gas phase aggregation, plasma polymerization and magnetron sputtering is laid, whereas in the second one the experimental setup and used methods are described. In the third and last chapter, we present obtained results and provide their extensive discussion.

At this point it is worth noting that the objective of this thesis is not to perform a comprehensive study of gas-phase synthesis of metal/plasma polymer nanoparticles, but rather a case study of certain selected systems.

1. Gas-phase synthesis of nanoparticles

Synthesis of nanomaterials can be divided into two groups:

1. top-down methods,

2. bottom-up methods.

The first ones denote for methods that start from bulk materials and use different procedures and techniques to modify them on nanoscale while using devices that are much larger and controlled externally (e.g. photolithography). In general, all these techniques share controlled and targeted removal, modification or reassembly of material.

On the contrary, the bottom-up methods start from atomic or molecular material and form desired outcomes by adding up pieces together. The gas aggregation is just one example among others, but will be discussed in this chapter for better understanding of experimental work.

1.1   Gas-phase aggregation

A naive, but illustrative example of gas-phase aggregation is given by professor Haberland [13] who mentions a formation of a cloud over a mountain as an example of gas aggregation. When wind blows over a mountain, the air undergoes adiabatic expansion, the temperature is lowered and the moisture in the air condenses into a cloud. He pinpoints that for efficient condensation process low temperatures and condensation germs are needed. Furthermore, he states that the presence of ions can serve the process as well as one can observe in the cloud chamber. In this case the inspected particles ionize the surrounding molecules inducing condensation and thus making their trajectory visible.

For deeper understanding of gas aggregation, several theories were developed based on different assumptions, but giving useful insights into underlying processes. All following ones share an assumption of homogeneous nucleation, which means no nucleation sites are favoured. The formation and collection of nanoparticles takes place in several steps:

  I) "vaporization" of the material;

 II) formation of embryos;

III) condensation or growth of embryos;

IV) coagulation and formation of "aggregates";

 V) sintering (compact particles with domains);
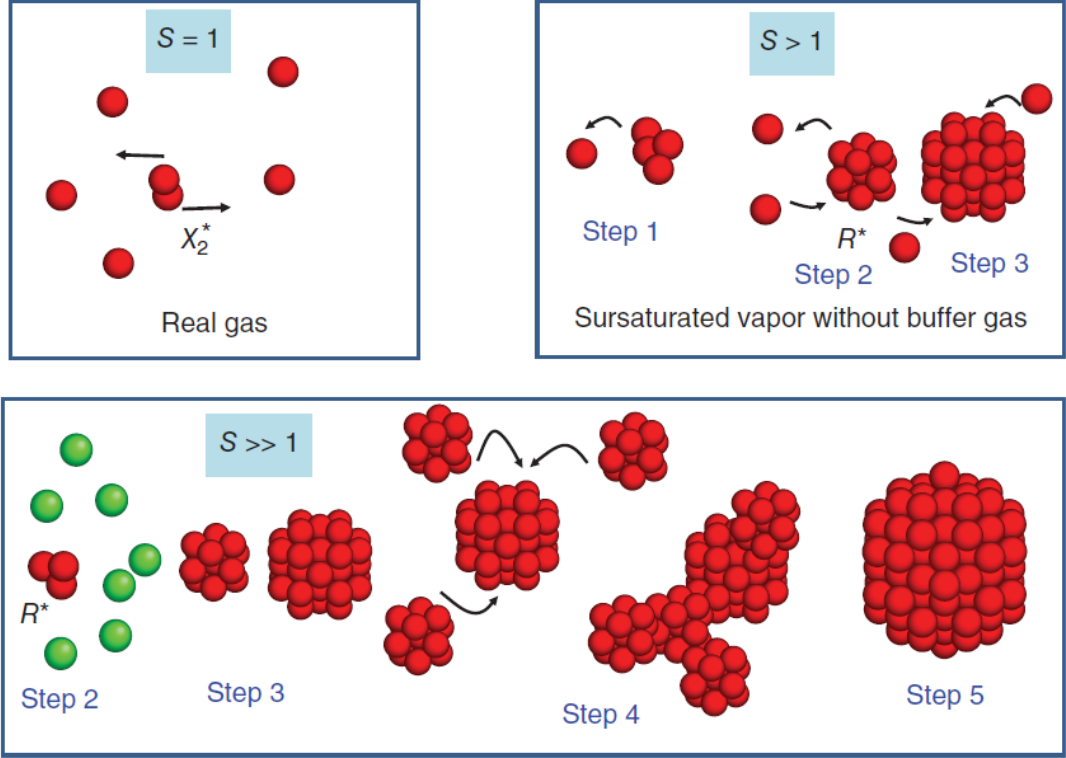
VI) transport and deposition of produced particles.

Figure 1.1: A schematic of three regimes of nucleation. S denotes supersaturation, R^* is critical radius. The figure is reprinted from [13].

These phases of formation of nanoparticles are schematically shown in figure 1.1. An important parameter S, which stands for supersaturation, is the ratio of pressure of a compound to its equilibrium vapour pressure. The picture indicates that for higher supersaturation the formation of particles becomes more effective.

The first step of the process (i.e. the production of the "vaporized" material) will be described later as there is a number of pathways how one can obtain vapour-like atomic or molecular material.

The following steps of the formation process are actually first-order phase transitions. Basic thermodynamic considerations lead to the van der Waals equation, which predicts an existence of critical pressure and temperature above which no phase transition occurs. From this it follows the demand for sufficiently low pressure and temperature in order to induce the phase transition.

Classical nucleation theory (CNT) states that the free enthalpy of droplet formation consists of two contributions. The volume term of free enthalpy is negative and decreases with the third power of radius (assuming the droplet has a spherical shape), whereas the surface term is positive and increases with the second power of radius. The CNT predicts the critical radius of nuclei

$$R^* = \frac{2\sigma\nu}{k_B T \log S} ,$$
(1.1)

where σ, ν, k_B, T are the surface energy, atomic volume, Boltzmann constant and temperature respectively. When the embryo reaches the critical radius, it is considered stable and can further grow in size. Moreover, from the CNT it

follows that nucleation rate J depends on the free enthalpy barrier ΔG:

$$J \propto \exp \frac{-\Delta G}{k_B T}, \tag{1.2}$$

which means that the nucleation rate slows down with an increase in the free enthalpy barrier.

However simple the CNT is and gives some hints about what governs the nucleation process, it cannot describe many systems precisely. Inaccuracies arise in smaller systems, because this theory assumes same properties for bulk material as for small clusters. In addition, for small clusters the meaning of temperature is rather a vague term.

To deal with some of the issues of the CNT, kinetic nucleation theory approach can be adopted. We can describe the nucleation as a two-step reaction:

$$X_{N-1} + X \overset{k_f(N)}{\underset{k_d(N)}{\rightleftarrows}} X_N^{\ddagger} \overset{p_s(N)}{\rightarrow} X_N. \tag{1.3}$$
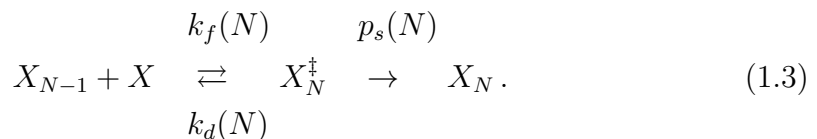
In the first step, there is the formation of a complex $X_N^{\ddagger}$ by adding a monomer to the embryo (with the probability $k_f(N)$). In the next step, the complex can be either destructed (with the probability $k_d(N)$) or stabilized by buffer gas or monomers (with the probability $p_s(N)$). In order to promote the growth of nanoparticles it is necessary that the lifetime of the complex is at least the same magnitude or larger than the time that is necessary to stabilize the complex.

Coming from theoretical models back to a lab, moderate supersaturation can be achieved through the adiabatic expansion of the "vaporized" material. In this case, which is also called supersonic expansion, the vapour of the desired material exits through an orifice and reduces its pressure. This leads to drop in the temperature and oversaturation and condensation can start.

The supersonic sources are based on the principle described in the previous paragraph and they were the first techniques explored for cluster production, but they are not able to form an intense beam of nanoparticles on their own. As an aid to this, a buffer gas can be used that helps to reach the critical radius faster. Adding additional substance that does not participate in nucleation and growth is especially useful for releasing the vibrational energy and therefore for stabilizing the clusters. [13]

1.2   Haberland type of gas aggregation source

The ways and means how "vaporized" material can be produced are numerous (e.g. Joule heating, laser ablation, pulsed microplasma, arc discharge, etc.), although for the work presented here the magnetron sputtering is especially important.

Magnetron sputtering belongs to physical vapour deposition techniques, initially developed for thin film deposition. It originates from the observation that in gas discharges the material of a cathode is released and is accumulated on walls. To enhance the efficiency of sputtering the electrons are confined by electromagnetic field and follow helical paths. Because of their localisation, higher

ionisation rates are observed in the near of the cathode. Ionized species of the working gas are then accelerated towards the cathode and the bombardment of the target attached to the cathode occurs and the material is "vaporized".

The idea to use magnetron as a source of material for gas-phase synthesis of nanoparticles came in early nineties from professor Haberland and his co-workers in Freiburg, Germany. [1, 14, 15, 16] The original set-up developed by this group is presented in figure 1.2).
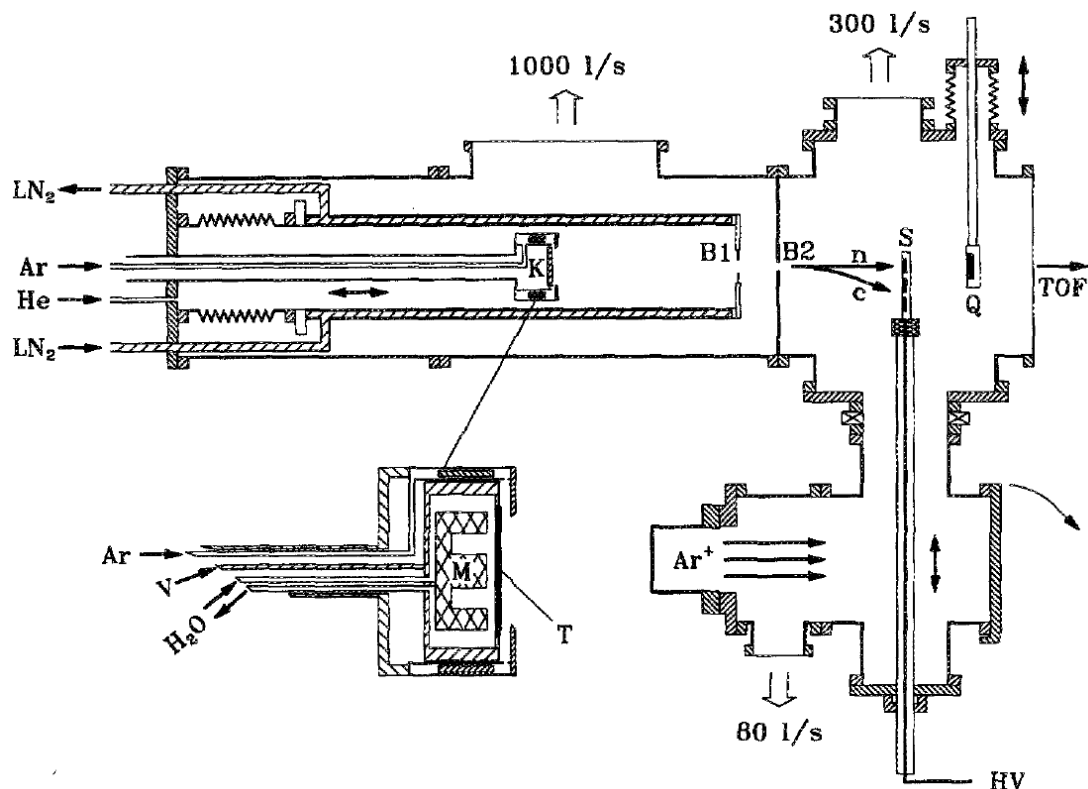

Figure 1.2: Gas aggregation cluster source developed by professor Haberland. The experimental set-up consists of several parts. The magnetron head K is contained in a chamber cooled by liquid nitrogen. The clusters leave the aggregation chamber through two-diaphragms B1 and B2 and can be deposited on a substrate S or their sizes can be monitored by a mass spectrometer TOF. The beam intensity can be monitored by a microbalance Q. The bottom part of the deposition chamber with Ar^+ was used to clean substrates. The figure is reprinted from [16].

The main part of the whole apparatus is a planar magnetron placed inside an aggregation chamber. The magnetron K consists of magnets M and target T, both water cooled. This is concealed in an aggregation chamber which is cooled by liquid nitrogen and ended by two-diaphragms B1 and B2. The clusters were deposited on a substrate S and/or examined by characterization methods. A differential pumping system creating a pressure difference between the aggregation chamber and the deposition chamber was employed.

The main advantages of using a magnetron-based gas aggregation source lies in its high versatility, such as the range of the materials that can be used, high efficiency of clustering due to high concentration of dimers, wide range of produced particle sizes, a large percentage of ionized clusters that allows for control

of velocity/energy of produced nanoparticles and their mass/size filtration, and last, but not least, compatibility with other vacuum deposition techniques that enable production of complex nanomaterials.

The Haberland original concept can be modified in many ways, for example the power can be supplied with direct or alternating current (often the frequencies are chosen in radio-frequency (RF) range), in short pulses (with high power density, i.e. HIPIMS), an additional gas can be introduced to chamber leading to reactive sputtering or the pressure and selection of the working gas can be varied. [13, 17, 18]

Production of metallic nanoparticles by means of gas aggregation sources is already widely explored field with several published books and reviews, beside numerous articles. [13, 17, 19] The first clusters produced by Haberland's group were made of molybdenum, aluminium and copper. [15] Later, it was shown that it is possible to prepare metallic nanoparticles out of many materials like aluminium, ruthenium, tungsten, titanium, cobalt, silver, gold, copper, silicon or iron. [4, 20, 21, 22, 23, 24, 25, 26, 27]

The system can be further modified for the production of more complicated systems (e.g. alloy, Janus, dumbbell, core@shell, etc.). For instance, Llamosa and his co-workers put three magnetrons with metallic targets in one aggregation chamber and fabricated onion-like metal nanoparticles. By varying the relative positions of the magnetrons they were able to change the composition and layering in the nanoparticles. [7, 28] Another option is to use a single magnetron and a composite target, which was done for example by Xu and Wang who fabricated FeCo alloy and Co-Au core@shell nanoparticles. [29, 30]

Third pathway of producing heterogeneous or more specifically core@shell nanoparticles is so called in-flight modification. This approach separates the fabrication into two independent steps that can be controlled individually. At first, the core particles are formed and exit the aggregation source. In the second step, they fly through a zone where their surface can be modified or coated, for example, in a second discharge. For instance, at the Department of Macromolecular Physics, such nanoparticles were produced combining nickel with titanium and nickel with copper. [31, 32]

1.3   Plasma polymerization

Another class of materials constitute so-called plasma polymers. Such materials, unlike the conventional polymers, do not have regularly repeating units. Albeit, similarly to conventional polymers, there may be monomer units at the beginning, the structure of the produced material is rather complicated with a high degree of disorder and cross-linking, short chains and high amount of radicals implanted inside. An example of such a structure is shown in figure 1.3.

It is not only the structure what makes plasma polymers different from conventional polymers, but their attractive properties (chemical, mechanical and bioadhesive) can be recognized in a number of applications. For instance, they can be used for protective coatings with tunable wettability, permeation membranes or chemical sensory devices. [33, 34, 35, 36, 37] They can be also easily functionalized, which is very useful feature for biomedical utilization. [38, 39, 40]
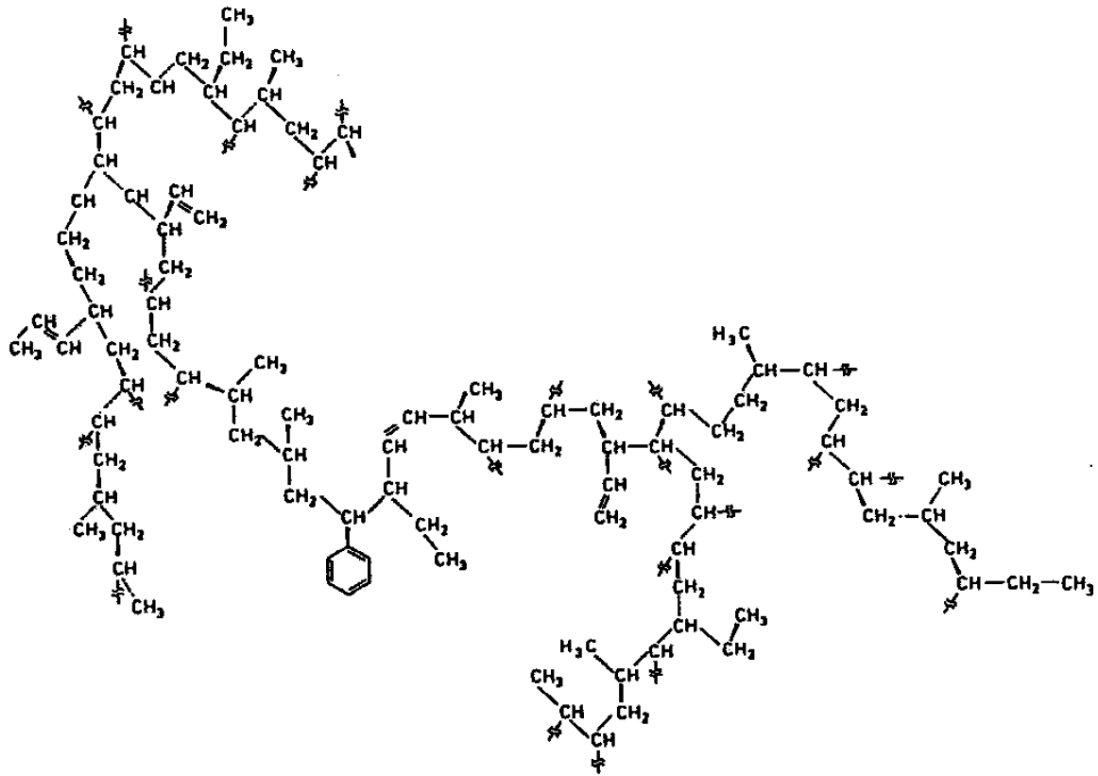
Figure 1.3: An example of how the structure of plasma polymer can look like. The figure is reprinted from [33].

Concerning the growth of plasma polymers, three distinct phases may be recognised:

  I) initiation;

 II) propagation;

III) termination.

At the beginning of plasma polymerization, precursors supplied into the plasma (e.g. in a form of organic vapours or as molecular fragments emitted from a polymeric target during its magnetron sputtering) are activated by plasma and various fragments, radicals and other species are created. These can further be transformed into products via chemical reactions, some of them contributing to plasma polymerization. An overview of the polymerization mechanism based on the rapid step-growth principle is pictured in the figure 1.4.

The activated species (radicals) from the first step can follow in general two major possible paths (this stage is usually called as propagation of polymerization): in cycle I, the plasma polymerization proceeds via free radical growth polymerization from single radical species by shifting the radical center and leaving it open for further polymerization process, while in cycle II divalent active species are involved in the polymerization process. Moreover, a reaction that combines a single reactive species with a divalent reactive species in a cross-cycle reaction is also possible.

The growth can be also terminated, e.g. when an inactive species is formed and is not reactivated, plasma ceases or monomers become unavailable. [33, 41, 42]

Naturally, all three phases – initiation, propagation and termination – may take place both in the plasma volume or on a solid substrate introduced into or close to the plasma zone. However, in the case of conventional plasma polymerization that is performed at relatively low pressures, the propagation and termination predominantly occur at the solid/plasma interface. This gives rise to compact, smooth thin films of plasma polymers with good conformity.
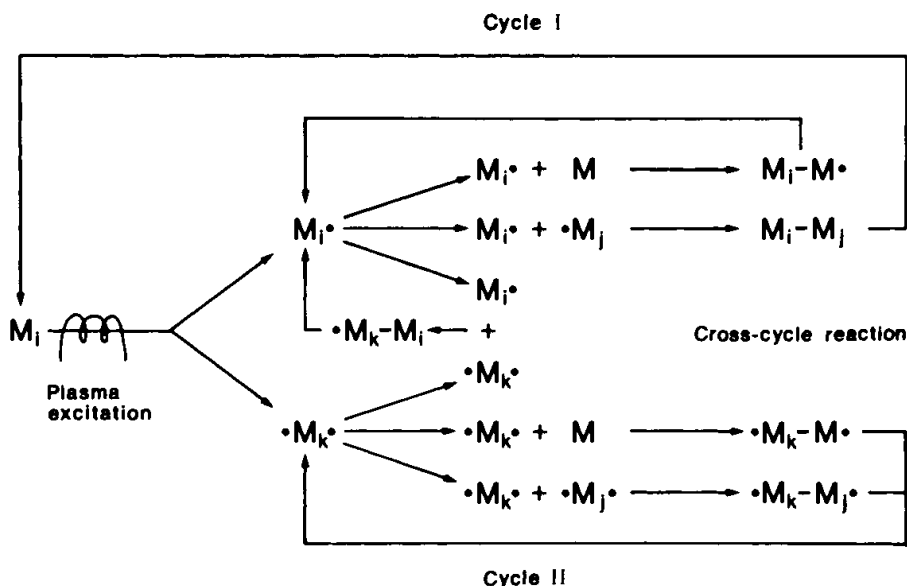

Figure 1.4: A diagram of bicyclic step-growth mechanism of plasma polymerization. The subscripts i, j, k indicate that the species may differ (in size). The figure is reprinted from [33].

The first reports on substances which we nowadays recognize as plasma polymers dates back to the second half of 18th century. Nevertheless, some time passed until more intense research started to appear. The real boom of plasma polymerization came in the sixties of the last century and it was realized that this approach is highly valuable especially when it comes to thin film production. [43, 44, 45, 37, 46]

However, at the same time, the formation of particulates via plasma polymerization was also perceived as a side product that was not really desired. This clearly pointed on the fact that at certain conditions, the propagation phase of plasma polymerization may occur in the gas phase. [8, 47, 48, 49] These studies also led to an origin of a new branch of physics, so called physics of dusty plasma. In this case, the plasma polymer particulates are seen as some kind of dust that interacts with plasma. Besides that, this field overlaps with astrophysics (for example interstellar clouds, the rings of the Giant planets or comet tails can be considered as examples of dusty plasma). [50]

Saying this, it is important to note that for long time the main interest in the field of dusty plasma was investigation of the mutual interactions of plasma and plasma polymer particles, while the possibility to use plasma polymerization for tailor-made production of functional plasma polymer nanoparticles was somehow overlooked. This was foremost connected with the difficulty to transport formed nanoparticles in a controlled way to the substrate. In a conventional arrangement

used for the production of plasma polymer nanoparticles, formed nanoparticles readily acquire negative charge and are trapped by electrostatic forces in the plasma volume, where they continue to grow. The principal force that is capable to surpass electrostatic forces and allow thus nanoparticles to escape towards the substrate is the gravity. This often means that only relatively big particles may reach the substrate. However, as it was demonstrated in the pioneering work of Biederman group [9], this limitation may be overcome, when Haberland type of gas aggregation source is used. Unlike in other arrangements, the flow of buffer gas is capable to force nanoparticles to leave the plasma zone and thus facilitate their deposition. Furthermore, it was shown that produced C:H:N:O particles had cauliflower-like structure and their size was decreasing with increasing power and increasing with the increasing residence time in the aggregation zone. [9] Some other works with similar experimental setup followed. [51, 52]

1.4 Synthesis of heterogeneous metal/plasma polymer nanoparticles

Although it is possible to create more kinds of nanostructures and nanocomposites, as myriad of published articles prove, the goal of this chapter is not to provide a comprehensive review, but to give an overall context of the accomplished experimental work.

In the previous two sections, we learned that it is possible to fabricate metallic and plasma polymer nanoparticles using gas aggregation sources. On the following lines, we mention some research papers that combine these two classes of materials (and we focus on the contributions from the Department of Macromolecular Physics).

Nanocomposite metal/plasma polymer films can be formed by sputtering of a metallic target and simultaneous plasma polymerization of gaseous precursors. In such a way, it was, for instance, possible to incorporate silver nanoparticles inside a C:H and C:H:N plasma polymer matrix. [53, 54]

When a better control over nanostructure and particularly nanoparticles has to be maintained, it is possible to use gas aggregation source and produce nanoparticles separately. These nanoparticles can be then embedded in a matrix or deposited on a substrate and overcoated by a different material. Such nanocomposite films were prepared, e.g. silver nanoparticles with C:H plasma polymer [55], C:H plasma polymer particles overcoated by titanium [56], titanium or copper nanoclusters with matrix made of sputtered nylon [57, 58], titanium or silver nanoparticles in plasma polymerized n-hexane matrix [57, 59], silver nanoclusters overcoated by magnetron-sputtered PTFE [60].

Recently, a number of studies appeared proving that it is also possible to combine both classes of materials in a single nanoparticle. Approaches that can be adopted are quite similar to those combining different metals. These methods include using of a composite target on a magnetron, more magnetrons in one aggregation chamber, combination of magnetron sputtering with plasma enhanced chemical vapour deposition in a single aggregation chamber at higher pressure or in-flight modification. [61] The first three practises do not allow independent variation of metal and plasma polymer in the final nanoparticle, be-

cause both types of materials happen to grow and form the nanoparticle at the same time and in the same region. For example, Solař and his colleagues studied formation of silver/plasma polymer nanoparticles when hexamethyldisiloxane (HMDSO) was added into the working gas mixture flowing through an aggregation chamber equipped with magnetron with silver target. As a result, produced cores were metallic, whereas the shell was made of plasma polymer. [11] Depending on the fraction of admixed precursor, nanoparticles with different structures were observed; while for low HMDSO concentration in the working gas mixture core@shell nanoparticles were produced, increase in the HMDSO concentration resulted in the formation of multi-core@shell nanoparticles of irregular structure.

However, the growth of both phases can be separated spatially and temporally. Kylián at al. used the gas aggregation source with a magnetron to produce copper nanoparticles that were covered by plasma polymer in an adjacent chamber. These authors were able to produce nanoparticles with thin and homogeneous plasma polymer shells without affecting the properties of the metallic core. [12]

Finally, it has to be stressed that in all so far studied cases of metal/plasma polymer nanoparticles, the cores were always metallic. In this context, it is thus interesting to test if the structure may be reversed, i.e. whether it is possible to synthesize nanoparticles with plasma polymer core covered by metal. In order to answer this question, which represents the central topic of this thesis, we have adopted a system similar to the one previously employed for the production of silicon/silver nanoparticles. [62] These authors divided the deposition apparatus into three zones: in the first one, the silicon core particles were formed by gas-phase aggregation, in the second part, the in-flight coating by silver was taking place and in the third zone, the final particles were collected on substrates.

2. Experimental setup

2.1   Apparatus for nanoparticle fabrication

For the fabrication of nanoparticles the setup from picture 2.1 was used. It was divided into three parts: in the first one (in the very left of the sketch) C:H:N:O nanoparticles were produced via gas aggregation, then they entered a zone where they were exposed to plasma with metallic species produced by magnetron sputtering of a target made of silver, titanium or copper. For the purposes of this work, we call this section of in-flight modification as the *inoculation zone*. The resultant particles were ejected into the main deposition chamber (in the very right of the scheme) where they were collected on various substrates. The initial idea was to separate the fabrication of the plasma polymer and metallic parts of the nanoparticle in order to vary the properties of each part independently.
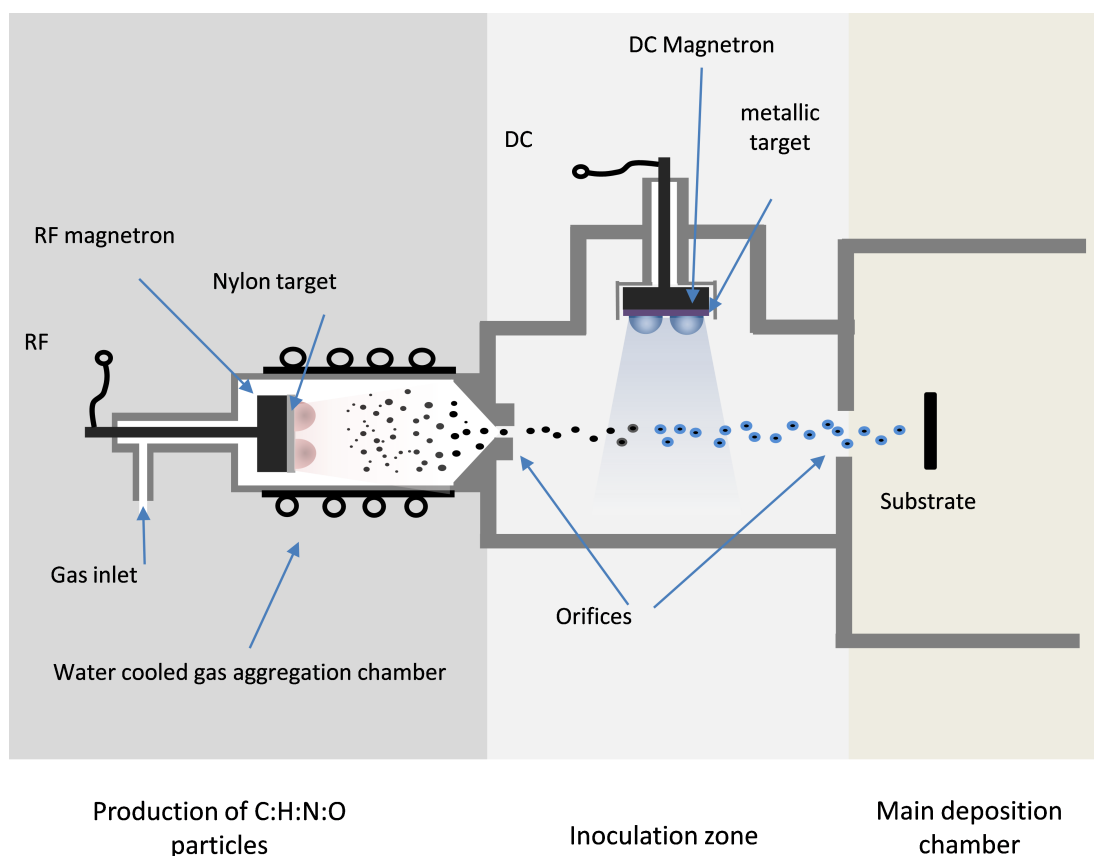
Figure 2.1: Apparatus for nanoparticle fabrication

The production of C:H:N:O nanoparticles took place in a water cooled gas aggregation chamber with inner diameter of 102 mm (in the picture 2.1 on the very left). The exit orifice (2.5 mm in diameter) was placed at the end of a cone on one side of the chamber and was leading to second aggregation chamber. Opposite to the exit orifice, there was a RF planar magnetron with a 2 mm thick target made of Nylon 6,6 (diameter 81 mm, producer: Goodfellow). Argon atmosphere was introduced to the chamber behind the magnetron, the gas flow was regulated via gas flow controller up to 30 sccm (which corresponds to 125 Pa). RF power

was supplied by a power generator (Dressler CESAR Generator, Model 1310) via a matching box.

The produced plasma polymer nanoparticles travelled through an orifice to the inoculation zone, which was also a gas aggregation chamber, but this time the DC magnetron was placed perpendicular to the direction of travel of nanoparticles (see figure 2.1). The distance between the axes of the particle beam and the silver, copper or titanium target (3 inches in diameter, 3 mm thick, producer: Safina or Kurt J Lessker) was 60 mm. The flow of 28 sccm corresponded to 55 Pa in this chamber. The chamber was terminated with 3 mm orifice.

The resulting nanoparticles were then transported to the main deposition chamber where they were deposited on various substrates. The samples were introduced into this chamber via a load-lock system pumped by a rotary pump. The pressure in the main deposition chamber was kept in the units of pascals, around 5.5 Pa for most experiments and the pumping was arranged by rotary and diffusion pumps.

2.2 Quartz crystal microbalance

Quartz crystal microbalance belongs to gravimetrical methods and is suitable for in situ monitoring of small deposited mass. It measures the change of resonant frequency, which can be recalculated to the mass variation. When there is some material deposited on the crystal, its resonant frequency decreases and for small changes this dependency is linear. [63] This measurement was first introduced by Guenter Sauerbrey, who also derived the equation bearing his name and describing the technique precisely:

$$\Delta f = -\frac{2f^2 \Delta m}{A\sqrt{\rho\mu}} \, , \tag{2.1}$$

where f is the resonant frequency, Δf its change, Δm mass increment, A active area of the crystal, ρ crystal density and μ shear modulus of the crystal. This approach is treating the deposited material as an extension of thickness and further conditions has to be met to make a valid interpretation of data: the material deposited on the crystal must be rigid, homogeneously spread over the surface and the frequency change must remain small. [64]

The initial frequency of the custom made QCM system that uses gold-coated Si disks was 5 MHz and the sampling frequency was 1 Hz.

2.3 Optical emission spectroscopy

Due to its nature, the plasma contains excited species that are able to emit photons. The energies of such photons are specific for each kind of an atom or a molecule and thus can be seen as unique fingerprints of species in plasma, because the energies or the wavelengths are proportional to the differences of thier energy levels. Optical emission spectroscopy is able to detect this light and by the interpretation of measured data we are able to monitor some of the excited species and therefore to get an insight into the processes inside the plasma without influencing its properties. [65]

In our measurements, the spectrophotometer Avantes Avaspec 3648 was employed and was connected to a computer and controlled by a software called Avasoft. This spectrophotometer was used for monitoring the processes in the plasma polymer gas aggregation chamber (the very left one in the figure 2.1). We measured whole emission spectra as well as the time evolution of intensities for chosen spectral bands (argon line: $841.8 - 842.8$ nm, CN band: $387.3 - 388.4$ nm). The background was always measured and subtracted.

2.4 Laser light scattering

If we place an object into a beam of light, we can observe several effects. The interactions between the object and the electromagnetic wave can happen in an elastic or inelastic manner. Both types are reducing the energy contained in the incident beam, and thus this phenomena can provide some useful information about the objects in the pathway of photons when the parameters of used light are known.

For description of elastic scattering, Mie theory was developed as the solution of Maxwell equations. Depending on the size of the object in the path of the electromagnetic wave, the solution can be divided into three sections: Rayleigh scattering, Mie scattering and geometric scattering. When using a laser with the wavelength in the visible region and probing the particles of nano- and submicrometer size, the first two play a significant role in what we observe. [66, 67, 68]
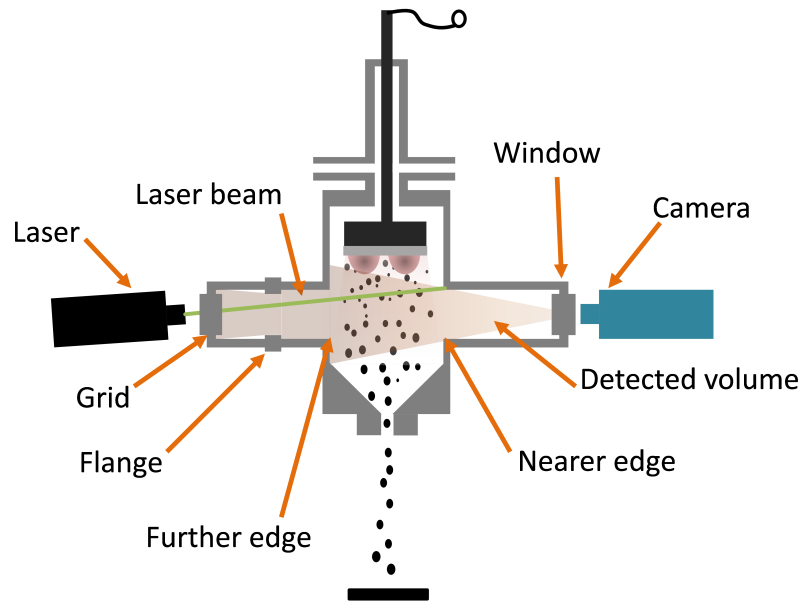
Figure 2.2: Apparatus for the laser scattering experiment

For laser light scattering experiments a laser of wavelength 532 nm and maximum power 450 mW was used and the laser beam was entering the plasma polymer gas aggregation chamber through a window with a grid. Inside the chamber the laser beam formed a 2D plane, which was oriented 7° above the horizontal level and thus hitting the upper nearer edge as shown in figure 2.2. The scattered light was collected by a high resolution CCD camera (Ximea, frame rate:

6 fps) equipped with a dielectric optical filter for the same wavelength as the laser light, which was placed in the opposite window to the window with the grid. The obtained data was further processed to eliminate the background and reflections from the walls and to enhance the signal via MATLAB software with a custom algorithm.

The scattering experiments were conducted at the Kiel University in Germany and thus some experimental details related to production of C:H:N:O particles had to be changed. The aggregation length was adjusted in the way that the target was aligned with the upper part of the edges, but was not crossing the laser plane. The chamber for the production of C:H:N:O particles was directly entering into the deposition chamber and so the inoculation zone was completely omitted for this set of experiments. The setup was pumped out by turbomolecular and scroll pumps and flow rate was adjusted in the way that the pressure inside the plasma polymer chamber was kept the same as in the experiments conducted in Prague.
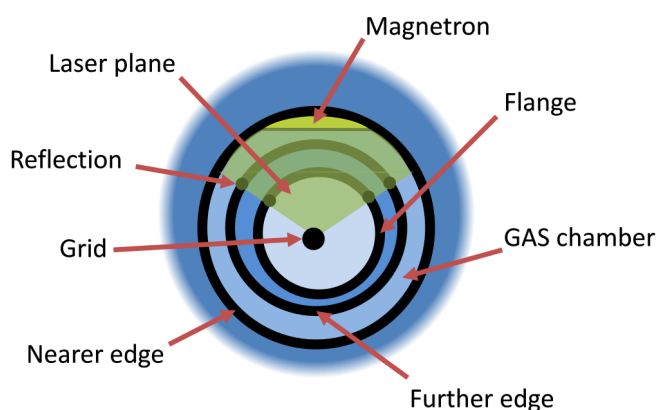
Figure 2.3: The camera view of the laser scattering experiment

In the picture 2.3 there is the camera view into the plasma polymer aggregation chamber. Each black circle represents an edge or a flange dividing the volume of the chamber into sections and each part can be also found in the figure 2.2. The main area where we expected some particles to appear is in between the edges and under the magnetron as there is the shortest path to the orifice. Because of the tilt of the laser plane upwards we awaited the signal to be coming from the upper part of the camera view.

2.5 Spectroscopic ellipsometry

Optical characterization methods can provide us with a quantity of information. Spectroscopic ellipsometry is a very good example of it. Via measurement of the change of polarization state and phase shift of light interacting with a thin film one can obtain the values of film thickness and many other optical constants. During the measurement, the light passes from a source through a couple of optical elements, which define the initial polarization of the wave. Then the light reaches the sample and interacts with it and refracted light travels again through another set of optical elements into a detector and the change of the polarization state and phase shift is obtained.

The acquisition of the data is just one part of all the effort and the measurement has to be followed by the evaluation of the data set. This is usually done by constructing a mathematical model and comparing it to the actual data. The final parameters of the model can be then interpreted as film thickness, index of refraction and possibly many other constants describing the original sample.

The spectroscopic ellipsometer Woollam M-2000DI and software CompleteEASE was used for measurement and fitting in this study. The wavelength range was $192 - 1690$ nm, the measurement was done at the angles of $55 - 75°$ and samples were supported by one side polished silicon wafers.

2.6 Electron microscopy

Electron microscopy is a technique that uses an accelerated electron beam to provide us with the information about the structure of a specimen. Due to the much shorter wavelength of the beam source, it is possible to reach much better resolution than with optical microscopy. This technique has two main types: scanning electron microscopy (SEM, the signal is acquired in the same half-space where the incoming beam is located) or transmission electron microscopy (TEM, the beam passes through the probed object and the signal is obtained in the half-space behind the object).

When the electron beam reaches the sample many processes happen in the interaction volume creating many kinds of species (e.g. backscattered electrons, secondary electrons, Auger electrons, characteristic X-rays, Bremsstrahlung, etc.). Depending on the type of the detector and its location we can examine the consequent signal and determine features related to topography, structure or chemical composition. [69]

The SEM measurements were done on the Tescan MIRA 3 microscope and Jeol JSM-7200F Schottky field emission scanning electron microscope. The TEM analyses were conducted on the JEOL2200FS microscope. [1]

As substrates, one side polished silicon wafers and TEM grids (Holey SiO Coated 300 Mesh Copper Grids) were used for SEM and TEM experiments respectively.

2.7 X-ray photoelectron spectroscopy

For determination of chemical composition, a method called X-ray photoelectron spectrometry is oftentimes used. An X-ray source produces photons of specific energy $h\nu$ and these photons interact with specimen and induce photoelectric effect. As a result, electrons with various energies do leave the sample and their kinetic energies E_k are proportional to the binding energies E_B in the atoms contained in the specimen in the following manner:

$$E_k = h\nu - E_B - \Phi \,, \tag{2.2}$$

where Φ is a work function of a particular spectrometer. From the chemical shift of the binding energies one can assess the types of chemical bonds.

Not all the electrons experience just this interaction, but a certain ratio is also scattered and adds to spectrum as a background. Although the penetration depth of X-rays can go up to several micrometers, the detected electrons come just from few nanometers and thus XPS can be used as a surface sensitive technique only.

The XPS analysis was conducted on Specs spectrometer equipped with an X-ray source XR-50 and a hemispherical analyzator Phoibos 100. Al Kα radiation of 1 486.61 eV was used. Wide spectra were taken in the region between 0 eV and 1 100 eV with pass energy of 40 eV. For the XPS analysis the samples were deposited on one side polished silicon wafers. All the data was processed with Casa XPS software.[2]

2.8   Ultraviolet-visible spectroscopy

Ultraviolet-visible (UV-Vis) spectroscopy is used for measuring optical transmittance or absorbance in the range of several hundred nanometres. The relationship between incident and transmitted light is described by Lambert-Beer law, which postulates that the absorbance is proportional to the concentration of absorbers (e.g. atoms, molecules), their molar absorptivity and the length over which attenuation occurs.

If there are metallic nanoparticles present in the sample, we can observe localized surface plasmon resonance (LSPR) in the UV-Vis spectrum. This phenomena is caused by light of a certain wavelength which causes the conduction electrons to oscillate coherently. [70, 71]

The spectrometer Hitachi U-2910 was used and measurements were done in the range of $192 - 1100$ nm. The samples for this analysis were deposited on soda lime glass.

---

[2]A huge thanks for the measurements goes to to RNDr. Jan Hanuš PhD.

3. Results and discussion

In this chapter, the experimental results related to the production of heterogeneous metal/plasma polymer nanoparticles are summarised and discussed. This chapter is divided into several sections. As we are employing a two-step process for creating heterogeneous nanoparticles that involves (i) production of plasma polymer cores and (ii) their subsequent in-flight coating by metal, we try our best in describing each of these steps separately in the first two sections. In the third part, we present the results of combining both steps together. Finally, we briefly report on using other materials and the same technique in the fourth section.

3.1 Production of C:H:N:O nanoparticles

The general aim of this study was to create heterogeneous nanoparticles with a two-step deposition technique. In the first step, a plasma polymeric core is formed and in this section we describe details of such production.
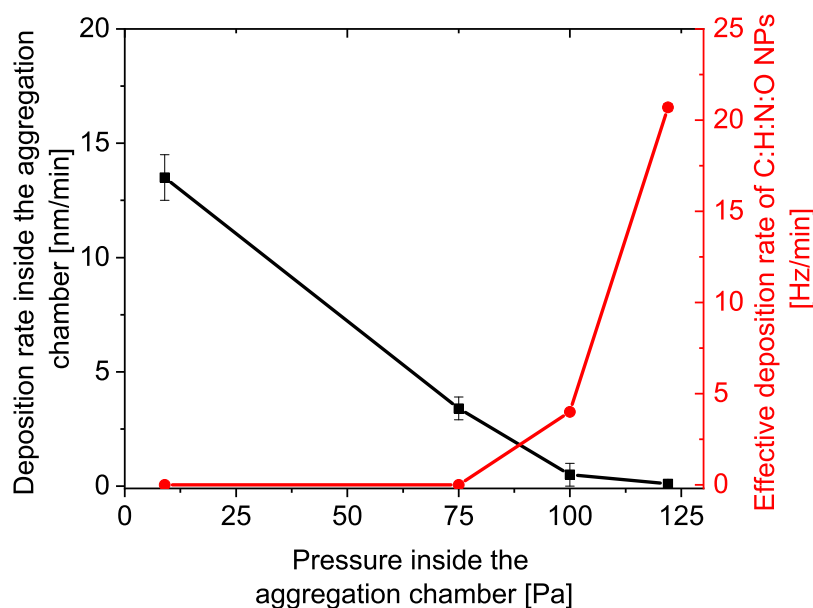
Figure 3.1: The comparison of the deposition rate inside the aggregation chamber and the effective deposition rate inside deposition chamber with respect to the pressure inside the aggregation chamber. Pressure in the main deposition chamber was 5.5 Pa.

Firstly, we needed to find the right conditions assuring the effective and reproducible fabrication of plasma polymer nanoparticles. For the sake of simplicity we will denote such nanoparticles in the subsequent text as C:H:N:O ones, which reflects their chemical composition.

An important parameter for gas-phase nanoparticle production is the pressure in the aggregation chamber. To study its effect on the processes in the aggregation chamber, we measured the deposition rate of material inside both, the aggregation and deposition chamber.

To evaluate the deposition rate inside the aggregation chamber used for the production of C:H:N:O nanoparticles, we placed a silicon substrate into it (see picture 2.1) for a specific time period and applied RF power of 40 W. Afterwards, we measured the film thickness with the ellipsometer and normalized it to the deposition time. This procedure was repeated for a set of pressure values. The data is pictured in figure 3.1 in black. We saw a consistent decrease in the deposition rate with increasing pressure and for the pressure values over 100 Pa very low deposition rate was observed.

Generally, there are two possible explanations of this effect: either the sputtering at higher pressures is not effective and thus only limited amount of material may reach the substrate and form a film, or the majority of the sputtered material is consumed during the production of nanoparticles that are subsequently transported by a working gas out of the aggregation chamber.

To test the aforementioned hypotheses, the deposition rate was measured by a QCM crystal that was placed in the deposition chamber facing the exit orifice. This time, we recognized an opposite trend to that of the first experiment. The deposition rate was negligible for the pressures below 100 Pa and started to rise rapidly for higher pressure values (see figure 3.1). This suggests that the hypothesis of material consumption for nanoparticles creation at higher pressures is correct. In other words, the formation of thin film is preferred for lower pressures, but as soon as the mean free path of species lowers down and collisions in the system become significant, the fragments prefer to form nanoparticles over impinging on a substrate. Such behaviour is similar to the production of metallic nanoparticles using similar gas aggregation sources.

Because the main goal of this part is to form plasma polymeric core particles in larger amounts, we chose the Ar gas flow of 28 sccm for further experiments as we observed the highest deposition rate for this value. This flow rate corresponds to the pressure inside the aggregation chamber of 122 Pa. If not stated otherwise, the power of 40 W was used in all subsequent experiments.

So far, we presented only the time-averaged deposition rates (in figure 3.1), but an interesting pattern was observed while we were monitoring the temporal variations of the deposition rate with QCM located in the deposition chamber. The data are plotted in figure 3.2. As can be seen, the deposition rate was not temporally stable, but resembled periodically repeating rectangular steps. This indicates that the C:H:N:O nanoparticles were leaving the aggregation chamber only at well-defined and relatively short time intervals and for the rest of the time the deposition rate was negligible.

In order to explain the observed fluctuations in the deposition rate, detailed analysis of plasma parameters was performed. First of all, it was found that the magnetron voltage oscillates with the same frequency as the deposition rate. This is demonstrated in figure 3.3, where time evolution of deposition rate is plotted together with the course of the magnetron voltage. It can be seen that the maximum of the deposition rate does correlate with the maximum of the magnetron voltage. This is marked in figure 3.3 by a grey dashed line.

Such behaviour may be explained as follows. First of all, the burst release of C:H:N:O nanoparticles suggests that the nanoparticles are trapped in the aggregation chamber for a relatively long time. Such trapped nanoparticles are readily charged negatively and thus act as an effective sink for electrons. When
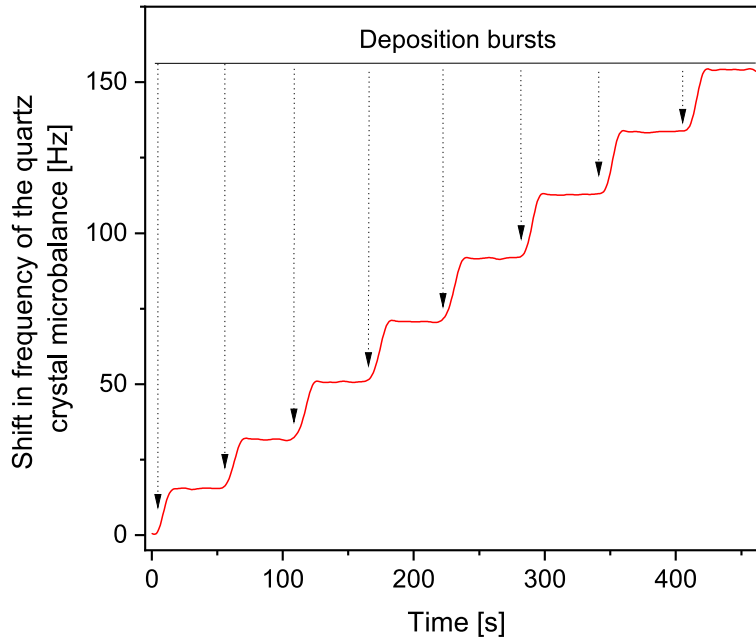
Figure 3.2: The shift in frequency of the quartz crystal microbalance (placed in the deposition chamber) as a function of time. The power of 40 W was used. The pressure in the aggregation chamber was 122 Pa.

a significant amount of nanoparticles is present in the aggregation chamber, the electron density starts to be smaller as compared to the positive ion density and the plasma starts to be more electronegative and resistive. [72] Because of this, the electric filed has to increase to sustain the plasma at constant applied RF power, which in turn causes an increase of both electron temperature and magnetron voltage. At this time point, the nanoparticles are released, the magnetron voltage drops and a new period starts.

For better understanding of the processes within the discharge, the optical emission spectra were acquired. A typical example of a recorded emission spectrum is plotted in figure 3.4. For longer wavelengths many argon peaks were detected as argon was used as the working gas. On the other side of the spectrum, the signal from CN molecules was detected. This material originates in the sputtering of nylon target. No other emission spectral bands or peaks were observed.

To probe again the stability of the discharge the time evolution of the intensities of an argon emission line at 840.8 nm and CN emission band at 388.3 nm were monitored. The data is shown in figure 3.5. Although a periodic behaviour can be observed for both of studied spectral systems, the courses of intensity variations with time differ markedly.

First, the intensity of Ar lines follows a similar trend as magnetron voltage. This is understandable as the argon does not participate in the formation of C:H:N:O nanoparticles and its density in the aggregation chamber stays constant. Because of this, the variation of the Ar line intensity reflects solely changes in the electron temperature or electron density in the plasma.

In contrast, the intensity of CN emission band includes also the information about the time variation of density of CN molecules in the plasma: the higher number of CN fragments in the discharge, the higher chance is to obtain the corre-
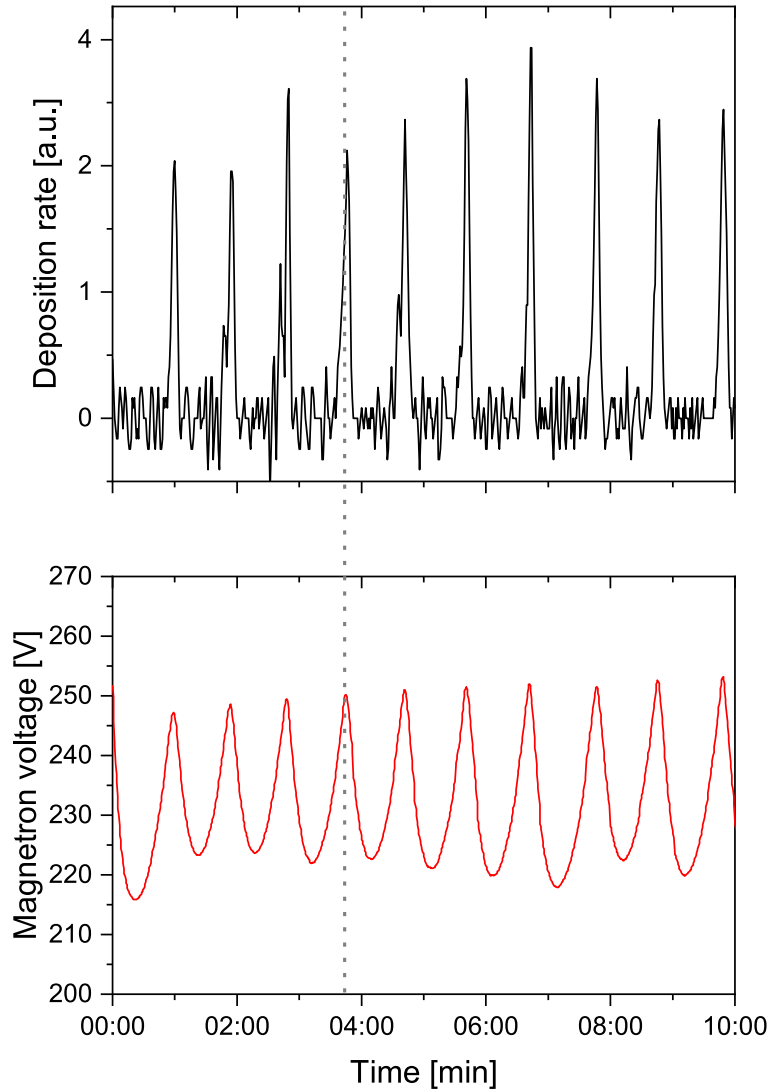
Figure 3.3: The time evolution of the deposition rate in the deposition chamber and the magnetron voltage (top and bottom graph respectively).

sponding signal from them. On the other hand, the CN fragments are consumed during the growth of the nanoparticles. Because of this, the number of CN fragments gradually decreases as the nanoparticles grow, which may explain observed decrease of the intensity of CN emission band. However, this depletion changes its slope over the time which can be linked to the particular growth phases. The first and faster part can be assigned to the rapid nucleation and coagulation phase in which the nanometer sized particles are readily created and form aggregates of the size of tens of nanometers. Later on, the growth slows down as the accretion takes place. At this phase the concentration of CN fragments still decreases but at much slower rate. [50, 73] The last drop can be attributed to the release of the particles.

The observed periodicity in the magnetron voltage, optical emission and deposition rate are the signs of a dusty plasma phenomenon called *growth induced instabilities* or *growth oscillations*. This theory explains the growth process of particles and connects the plasma reactions with it. In general, there is a number of forces acting on nanoparticles in plasmas: electromagnetic, gravitational,
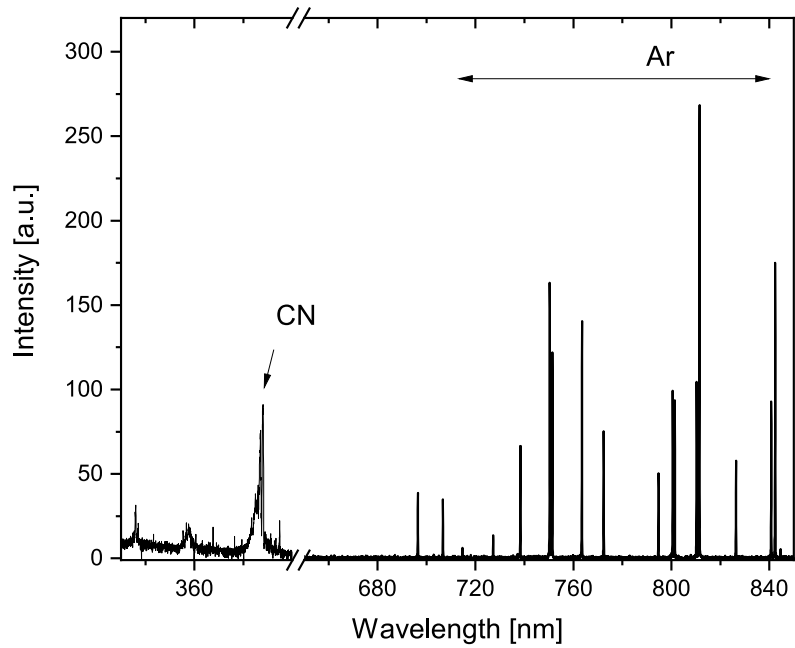
Figure 3.4: A typical example of measured wide optical emission spectra in the aggregation chamber.
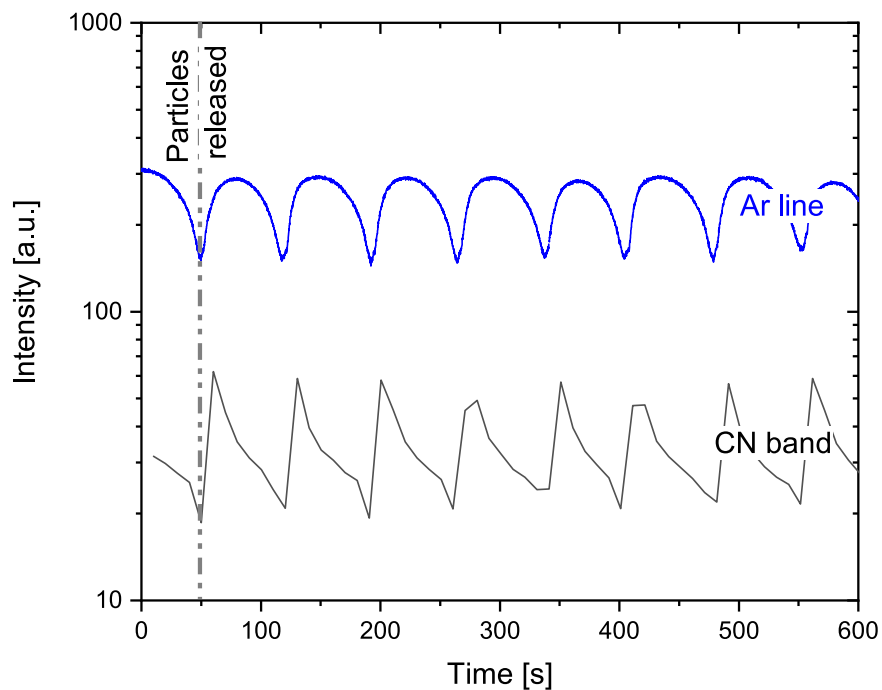
Figure 3.5: The time evolution of optical emission. The intensities of argon line and the CN band were monitored.

ion drag (interactions between ions and nanoparticles), neutral drag (a friction force caused by neutral gas) and thermophoretic force (caused by temperature gradient). Naturally, different forces have different directions: some of them force

nanoparticles to move into the plasma zone, while some of them act in the opposite direction. However, the forces acting on a nanoparticle scale up with the particle size r to its different power: electric force is proportional to r, ion drag, neutral drag and thermophoretic force are proportional to r^2 and gravitational force is proportional to r^3. For small nanoparticles the forces with direction into the plasma are prevailing and thus the nanoparticles are trapped in the plasma volume. [50, 74] However, as soon as the growing nanoparticle reaches a critical radius, the forces with the direction out of the plasma zone start to dominate and the nanoparticle is expelled from the plasma zone. [74]. At this point, a new growth cycle starts within the plasma and the discharge is quickly saturated with sputtered fragments, some of them serving as nucleation sites.
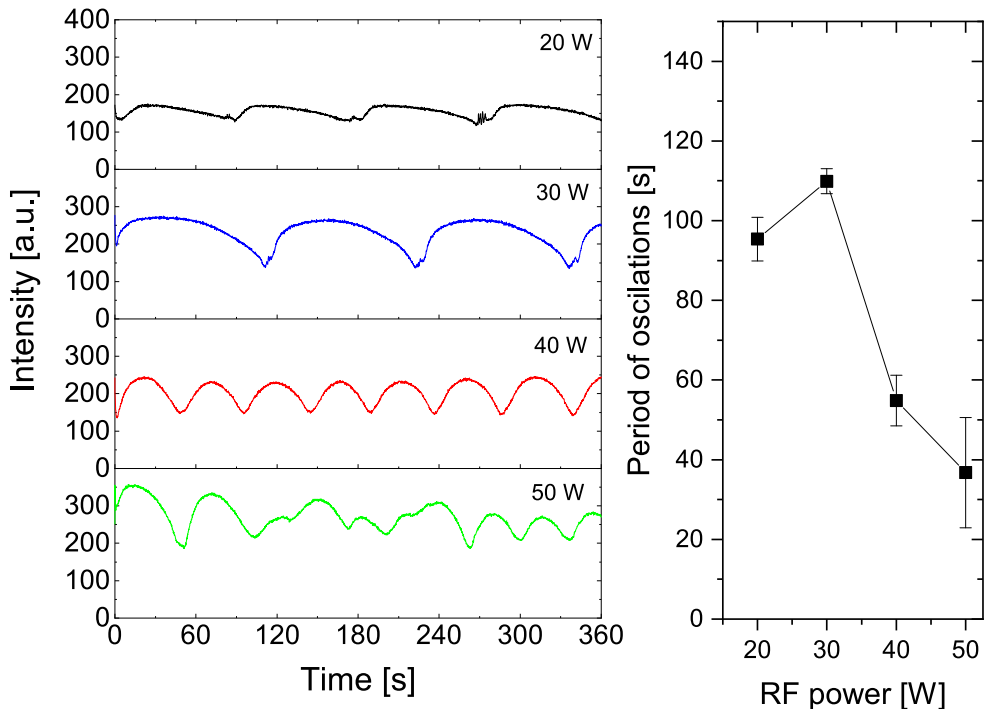
Figure 3.6: The left-hand graph shows how the intensity of argon emission line varies with time. The right-hand graph displays how the period of oscillation alters with applied RF power.

For the sake of completeness, we also monitored the periodic behaviour with respect to RF power. The data is plotted in the left-hand graph of figure 3.6. The argon optical emission was followed. In the right hand graph of the same figure, the average values of oscillation periods are displayed. Apparently, with higher powers the length of the growth cycle is decreased. It is likely that with the higher RF powers the particles reach the critical size (for which the forces become unbalanced) faster. It might be due to better availability of the building blocks, because it is probable that with higher powers the sputtering of a polymeric target is more effective. Additionally, it can be seen that the oscillations became irregular for applied RF power of 50 W.

In order to evaluate the physico-chemical properties of produced nanoparticles, set of samples was prepared at the discharge of 40 W and pressure of 122 Pa. SEM image of produced nanoparticles is presented in figure 3.7. The deposited particles have approximately spherical shape with little "bumps" on
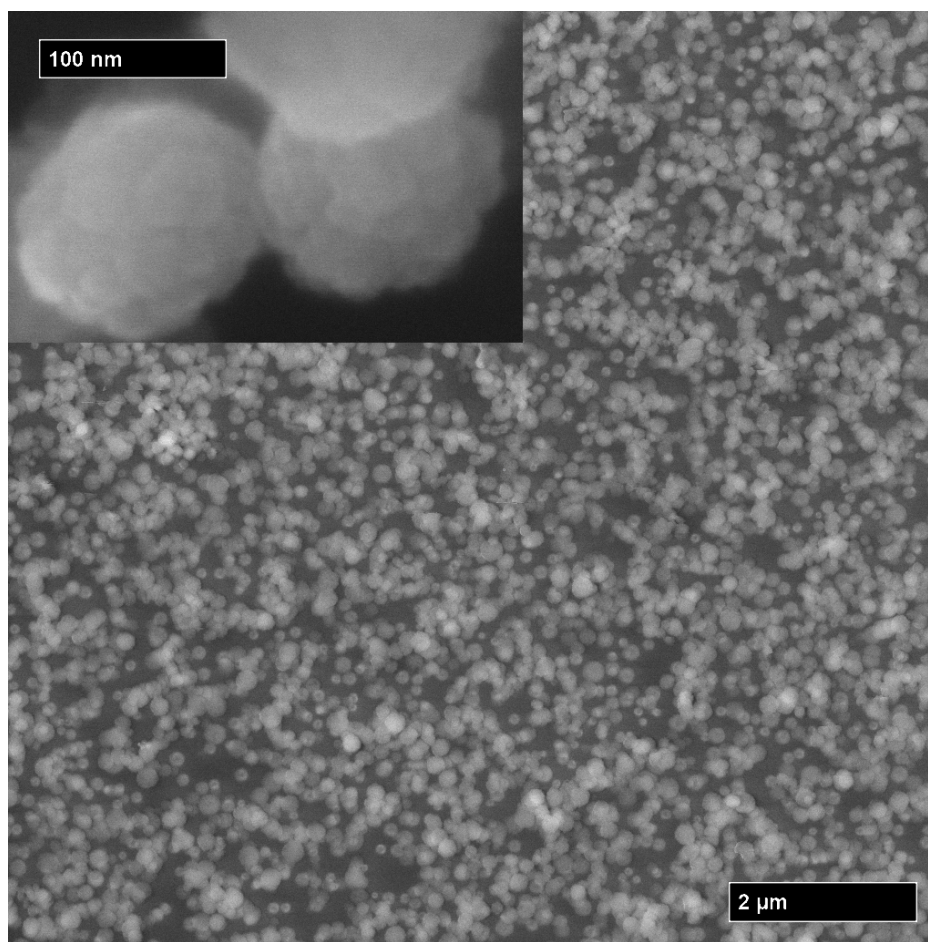
Figure 3.7: SEM image of the C:H:N:O particles for discharge power 40 W produced in Prague.

the surface. This is quite typical for plasma polymer particles and reflects their growth mechanism. At first the molecular fragments are joined to some kind of clusters which later coalesce into bigger agglomerates. Those clusters, however, may be manifested as protuberances on the particle surface.

By statistical evaluation of the SEM data sets, we obtained the particle size distribution as shown in figure 3.8. The deposited particle sizes ranged from the tens of nanometers to sub-micrometer values with the mean diameter of around (130 ± 30) nm and the size distribution was close to the Gaussian one.

The TEM analysis was done as well and an example is pictured in figure 3.9. The structure of individual particles is even more evident than in the case of SEM image: the agglomerates, which constitute the particles, are apparent and point to their formation process.

Finally, the chemical analysis of the samples was done by XPS. A survey spectrum was acquired and is shown in figure 3.10. Oxygen, nitrogen, carbon and silicon peaks were detected. Due to its low atomic number, hydrogen cannot be identified by XPS. The signal from silicon is caused by the substrate, because nanoparticles do not cover the whole surface as it is in the case of thin films. For this reason, part of the oxygen signal might be caused by silicon oxide that is usually present on the surfaces of silicon wafers. Similarly, a certain amount of
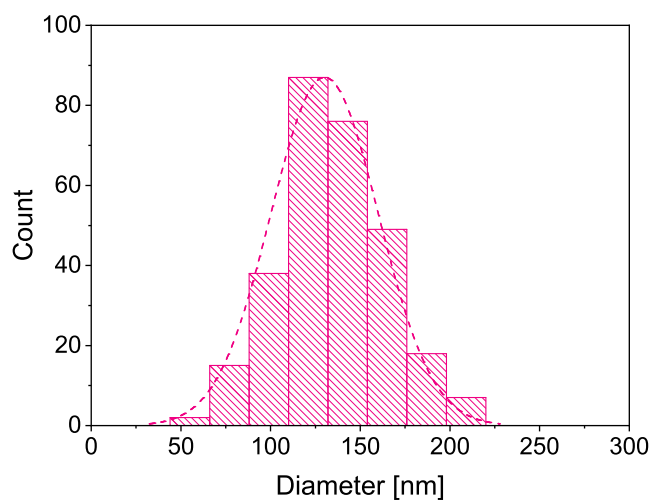
Figure 3.8: The size distribution of C:H:N:O particles formed at the power of 40 W. The mean diameter is (130 ± 30) nm.
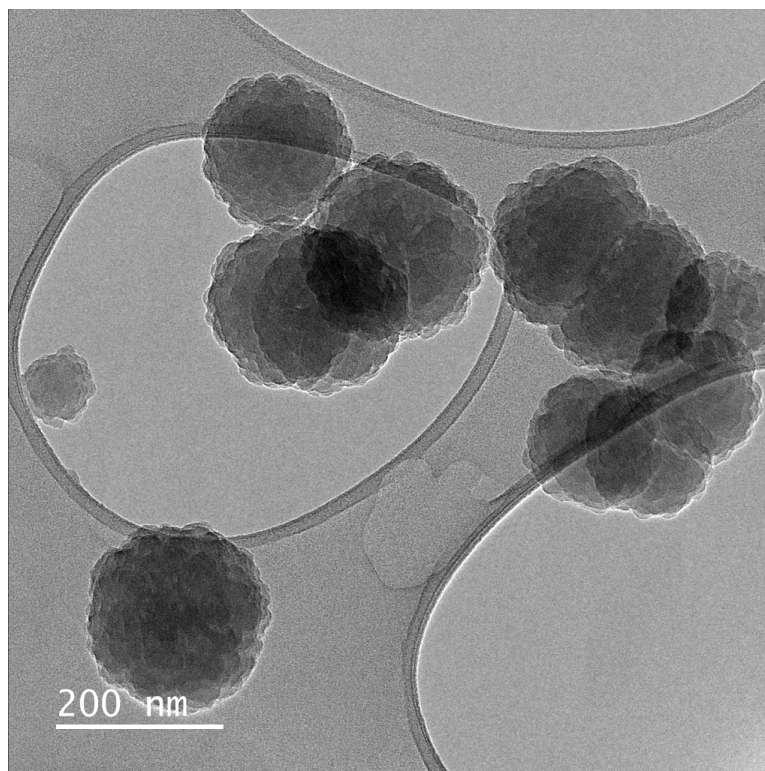
Figure 3.9: The TEM image of the C:H:N:O particles for discharge power 40 W.

carbon can be adsorbed on silicon surfaces when exposed to the atmosphere.[1]

The atomic concentration of species is as follows: C 40%, N 2%, O 15% and Si 43%. For a comparison, pure Nylon's composition would be: C 75%, N 12.5% and O 12.5%. When we look at the N/C ratio it is 0.17 for nylon 6,6 and 0.04 for our C:H:N:O nanoparticles. The lower fraction of nitrogen might be caused

---

[1]The XPS measurement was done ex-situ and the sample had to be exposed to air during the transport to the spectrometer.
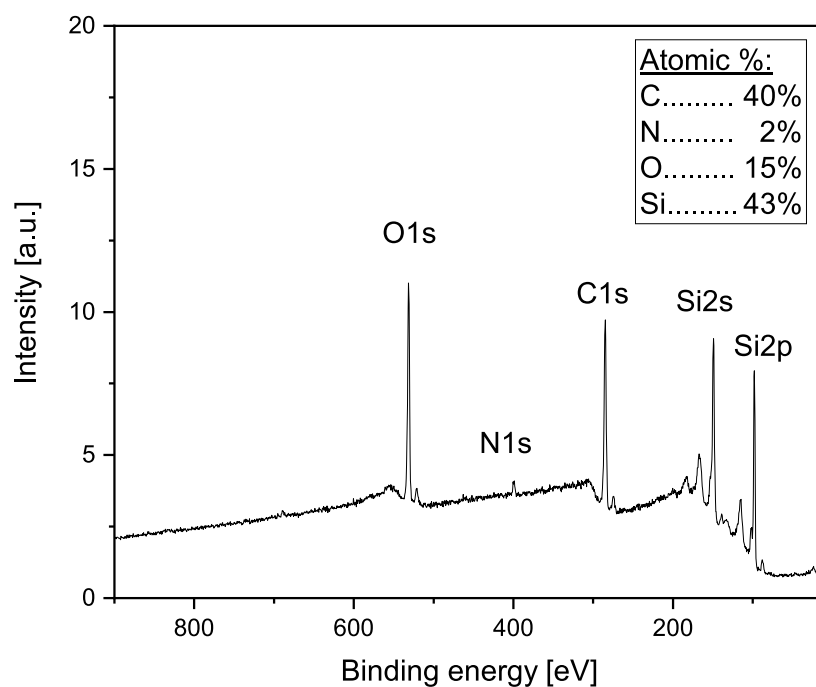
Figure 3.10: A survey spectrum of plasma polymer nanoparticles deposited on a silicon substrate with power of 40 W.

by the way, in which the nanoparticles are formed in the plasma. At this point, it is important to stress that during the plasma polymerisation, some volatile molecules and molecular fragments that do not participate in the plasma polymer growth may be created. Typical example of this is molecular nitrogen. Thus, it is possible that the atomic nitrogen that appears in the discharge reacts with another atom of the same kind forming molecular and gaseous nitrogen. This form of nitrogen is later pumped out from the experimental set-up and hence is not incorporated in the nanoparticles. It is also possible that other gaseous products are formed by other species.

On the other hand, lower percentage of nitrogen was not observed for thin films deposited by magnetron sputtering from nylon target at low pressure. [75, 46] Both works show comparable ratio to that of bare nylon 6,6. However, these thin films were produced at pressure values of two order smaller, which might suggest that the higher concentration of working gas in the discharge can significantly affect not only the clustering, but resulting chemical composition as well.

3.1.1 Laser light scattering

Although the results presented in the previous section indicated growth induced oscillation and trapping of C:H:N:O nanoparticles in the aggregation chamber, none of them directly confirmed this phenomenon. To prove the trapping, a different set of experiments was performed in a collaboration with Kiel University. For these experiments our plasma polymer gas aggregation chamber was installed on a deposition chamber available in Kiel. The processing parameters of the

discharge were kept comparable to the experiments conducted in Prague, the details are specified in the chapter 2.4.

At first, to check the performance of the gas aggregation source, the magnetron voltage was monitored with respect to time as it is shown in figure 3.11. The power coming to the discharge was set constant, which means that the magnetron voltage was adjusting itself in order to fulfil this requirement and thus reflecting in this way the processes within the plasma. Again, we observed voltage oscillations and consistently the period was shortening with increasing power. In general, the period of oscillations was shorter for Kiel experiments than for Prague ones, which could be assigned to slightly different geometry and conditions in this experiment. For example, the inoculation zone was missing, due to a different pumping system a bit higher argon flow had to be used in order to keep the same pressure inside the aggregation chamber, or because of the necessity to reduce the aggregation length for the scattering experiments. All these factors together can cause the difference of the discharge behaviour, but the general nature of it remained the same with growth induced instabilities playing an important role.
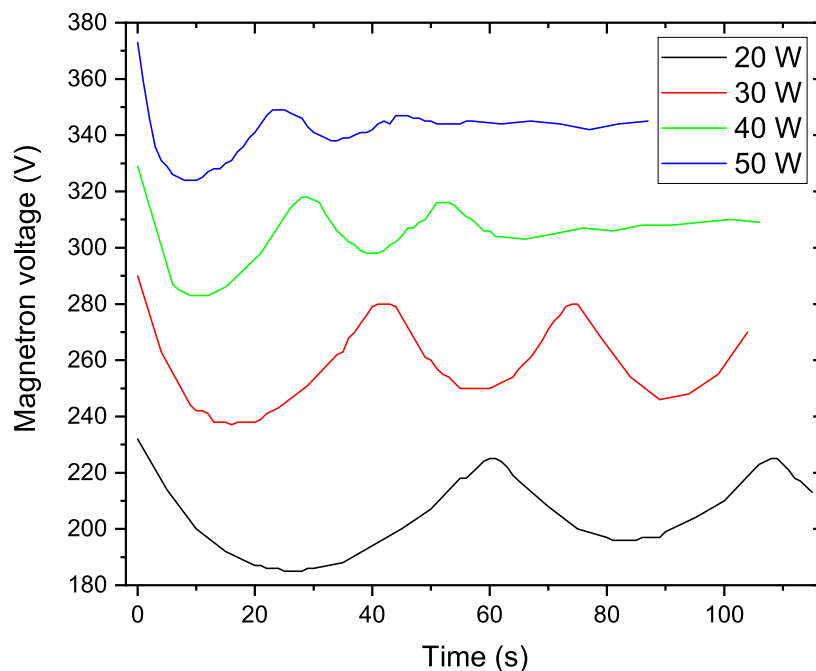
Figure 3.11: The magnetron voltage versus time for four different values of power.

Further comparison of performance of the gas aggregation source was focused on the size of produced nanoparticles. In this case we deposited particles on a silicon substrate at different applied RF powers. Every sample was subsequently investigated by SEM. An example of SEM image for 40 W is displayed in figure 3.12. The particles have round shape and do not seem to have wide size distribution. To quantify it, the size distributions were obtained as well. The results are shown in figure 3.13. Based on these results, two important findings may be drawn. At first, the sizes of produced C:H:N:O nanoparticles are somewhat smaller as compared to the nanoparticles deposited in Prague. This difference may be again ascribed to slightly different deposition conditions. Second interesting feature is a gentle increase of C:H:N:O nanoparticle size with increasing

power. This finding is contradictory to the results presented in the previous studies, in which an opposite trend was reported. [9, 76]
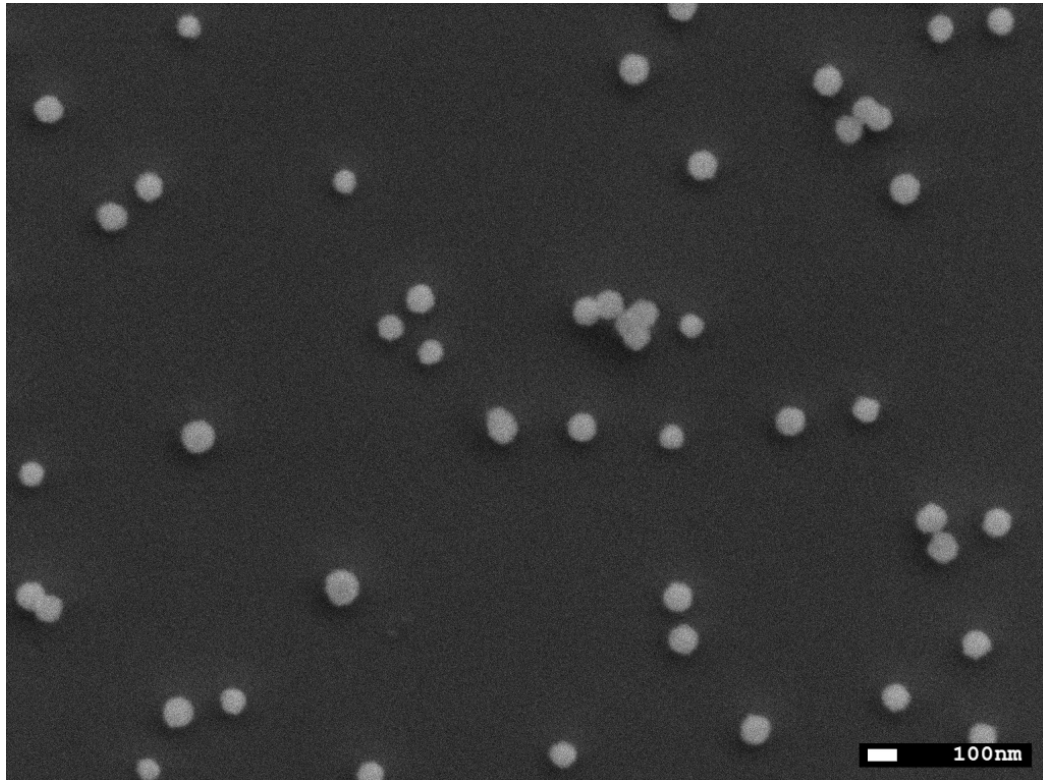
Figure 3.12: SEM image of nylon-sputtered particles for 40 W produced in Kiel.

One explanation for already published results says that with higher power the higher amount of material is sputtered. This leads to the higher probability of nucleation and thus greater number of smaller nanoparticles is formed. Here we can contend that the number of nucleation sites does not necessarily have to result in the same number of particles: if the agglomeration phase during the growth proceeds very effectively, the small clusters decrease their number density rapidly, while the number of bigger particles rises.

The second option might be the increased particle temperature. With higher power, the plasma density increases. This causes more electrons and ions to come to the surface of a particle and via recombination processes they release energy into the particle and heat it up. This excess of energy may result in the ablation of the particle. However, in this scenario the residence time of a nanoparticle in the plasma zone is not taken into account. Concerning the self-pulsing nature of nanoparticle production, we see that periods shorten with the increase of applied RF power. Hence, in the case of higher power the particle stays in the plasma zone for shorter time and thus is less heated/ablated as compared to the nanoparticles produced at lower powers.

In general, the production process of plasma polymer nanoparticles proceeds in the same fashion as in Prague. Therefore, the following laser light scattering experiments are relevant for better understanding of the growth process of such nanoparticles.

For the purpose of laser scattering experiments, four time points within the oscillation period were chosen dividing the period into four parts as pictured in
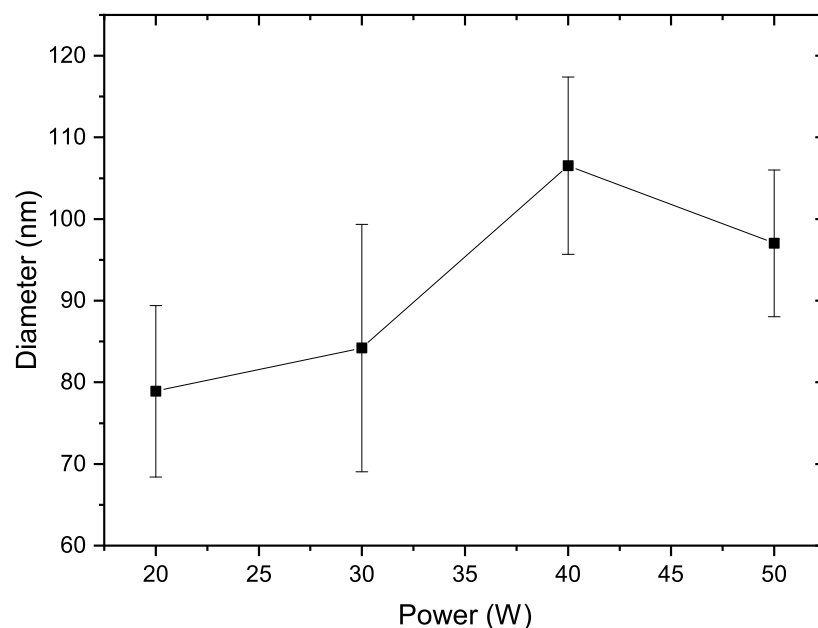
Figure 3.13: The mean diameter of the C:H:N:O particles produced in Kiel as a function of applied RF power. The error bars are representing the standard deviation of the ensemble.

the scheme 3.14. The point A is put at the beginning of the period when the magnetron voltage reaches the maximum and the point C was chosen as the minimum in voltage. The points B and D were set halfway in between.
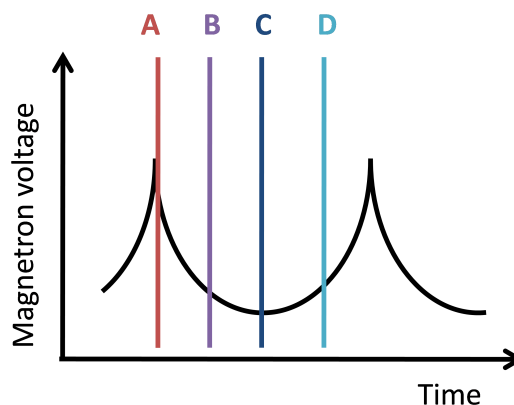
Figure 3.14: A scheme of the magnetron voltage oscillation with four marked time points within one period.

The light scattering experiments were conducted as follows: the discharge was run for one period and during the second period it was switched off in one of the time points. A video of the switching off and approximately following 10 s was captured and processed. This was done for all the time points A, B, C and D for powers of 20, 30, 40 and 50 W and hence creating 16 data sets in total. The picture 2.3 schematically describes how the acquired data should be understood.

The figure 3.15 shows a representative example of obtained pictures for 20 W. Each column is a set of subsequent frames for a particular time point indicated at the top of it. The very first photo was taken just before the switching off the

plasma and all the pictures in the column have a regular time spacing proportional to the frame rate as described in the section 2.4.

The time point A represented by the very left column in figure 3.15 is when the magnetron voltage peaks. From the earlier experiments, this culmination is connected to the release of the particles into the deposition chamber. The particles are therefore not present in the GAS chamber and are not able to cause a detectable light scattering.

The column B refers to the fast decrease in magnetron voltage during the first half of the period. In this phase of the period the optical emission of CN band reaches its maximum and the nucleation and formation of small aggregates is very likely to happen at this point. On the other hand, for the detection of light scattering the particles have to pass a certain size of tens of nanometers. [50] At this point, no signal could be observed, which is very likely when the particles are not sufficiently big.

In the next phase (the column C, the voltage reaches its minimum) some scattering signal is observable, which means that at this point the particles overcame the critical size for detection (approximately 50 nm for the used laser wavelength [50]). After the switching off, a toroidal cloud appeared in the laser sheet and was quickly reducing its diameter. The shape of the cloud suggests, that the particles are initially mostly concentrated above the race track. When the plasma switches off, the particles are released and travel towards the orifice. Why the diameter decreases can be the result of several factors: the particles can be dragged to the centre of the aggregation chamber by flowing working gas to some extent. On the other hand, the termination of plasma induces some other forces to play a role. For instance, due to the presence of charges, the ambipolar diffusion governs the disintegration of plasma and together with recombination processes can lead to a bit more complicated paths of the species and particles.

The last set of pictures (the very right column D of the figure 3.15) was taken when the voltage of the discharge was growing again. Also in this case nanoparticles were detectable and exhibited similar behaviour as in the case C. Thus, the same argumentation can be used for this case as well.

The suchlike data as described in previous paragraphs and displayed in figure 3.15 was taken also for powers of 30, 40 and 50 W. For all the experiments the scattering was expressed in the same dependence on the period phase. In figure 3.16 we show one frame for each power. This frame is the first snapshot taken after turning off the plasma as done in time point D (the magnetron voltage increasing with time). It is apparent that for higher powers the scattering becomes weaker. The intensity of the scattered light (for particles far from each other enough) is proportional to the size and amount of particles, so this finding suggests either variation of size of nanoparticles with applied RF power or their lower number for higher applied powers. However, three facts need to be emphasized at this point. First, for the higher powers the period of the oscillation is shorter and the switching off the plasma was not controlled by a computer. Therefore, the measurements that were performed at higher powers are less precise. Second, the stability of the oscillations at higher powers was lower and hence the growth induced instabilities can be less pronounced. Third, the intensities of the scattered light were evaluated only qualitatively and for a conclusion more accurate measurements should be done.
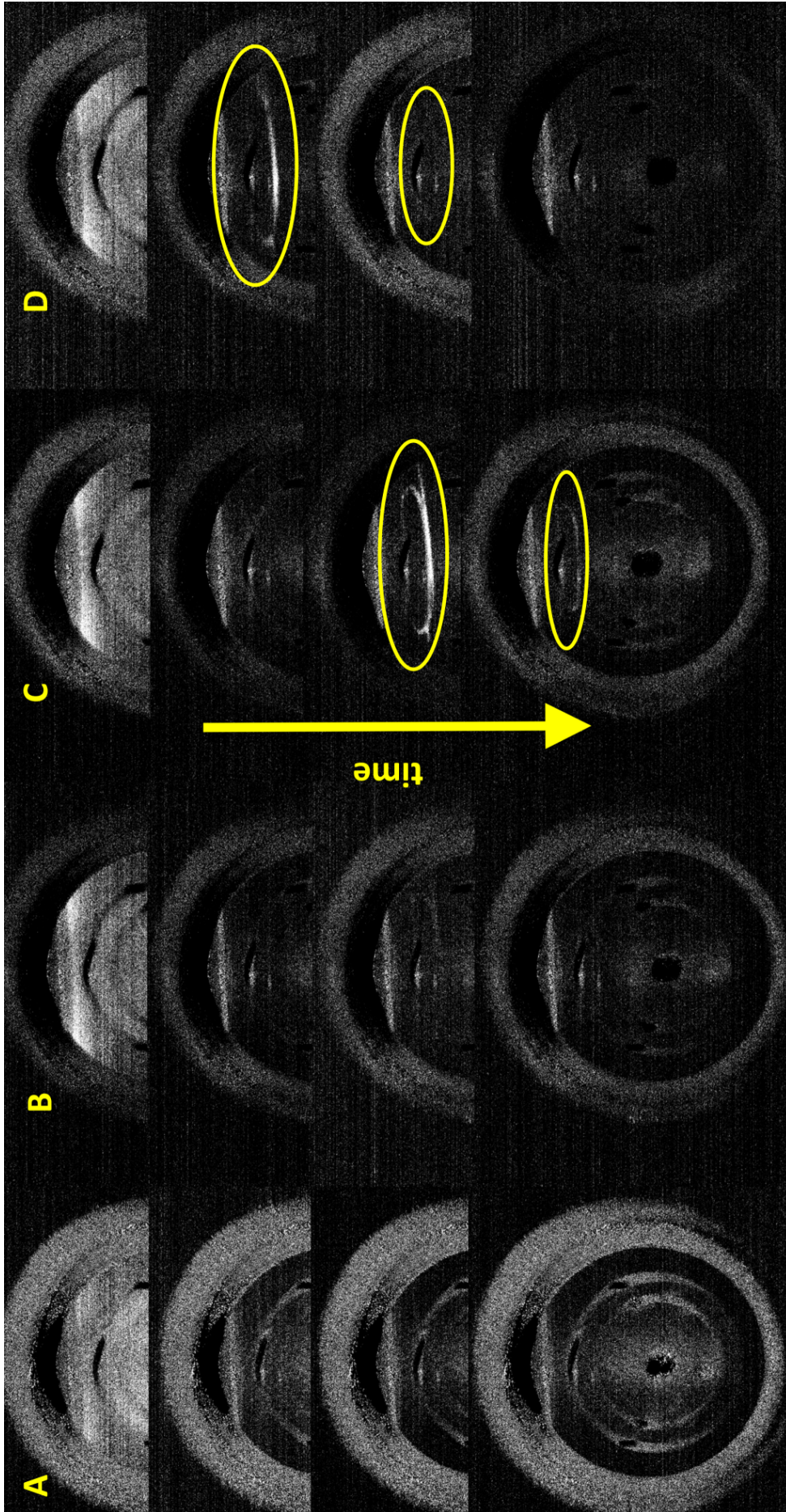
Figure 3.15: Four sets of photograph captured after turning off the discharge in four time points (see figure 3.14) during one discharge period. The RF power fed to the discharge was 20 W. Yellow ellipses mark toroidal scattering cloud.
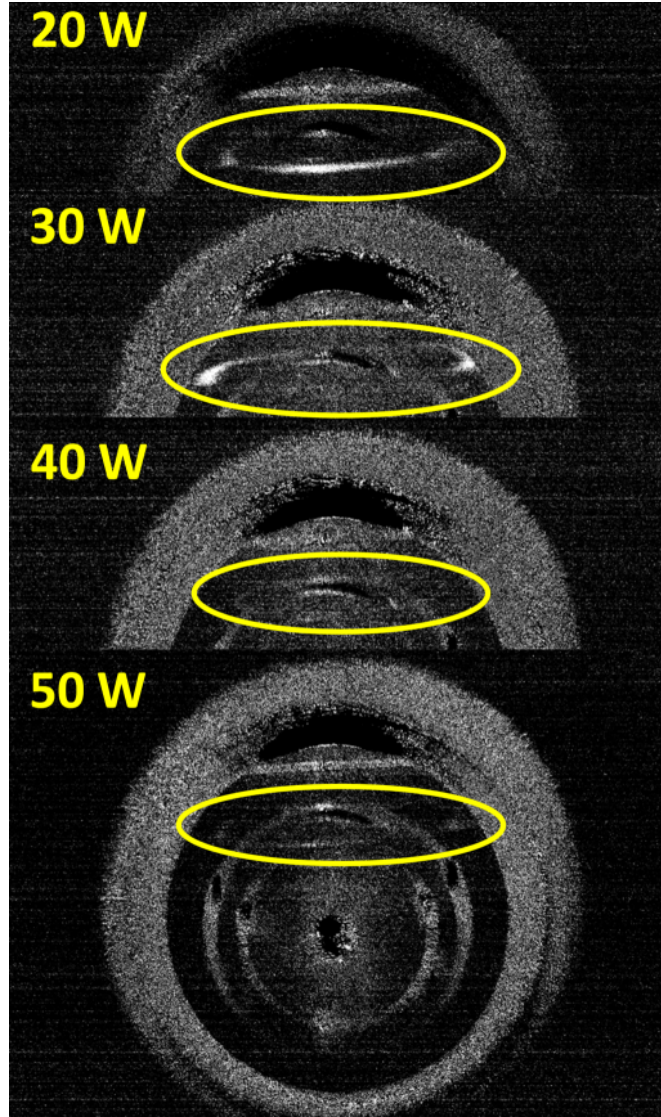
Figure 3.16: A toroidal cloud from the light scattering which was formed after switching off the discharge in the late phase of the period (marked as the time point D). Frames for all studied powers are shown. Yellow ellipses mark toroidal scattering cloud.

The evaluation of the torus diameter at different times after switching off the plasma was done and is shown in figure 3.17. We observed an exponential decay being almost independent on the RF power of the discharge. All the data was fit with just one exponential function to evaluate the general nature of this behaviour:

$$d(t) = d_0 \exp(-\alpha t), \tag{3.1}$$

where $d(t)$ is the diameter of the toroidal cloud, d_0 and α are fitting parameters and t is time after switching off the power supply. The fitting parameters were determined:

$$d_0^D = (47 \pm 3) \text{ mm},$$
$$\alpha^D = (2,4 \pm 0,2) \text{ s}^{-1}. \tag{3.2}$$

The parameter d_0 (or d_0^D) can be interpreted as the diameter of the torus when
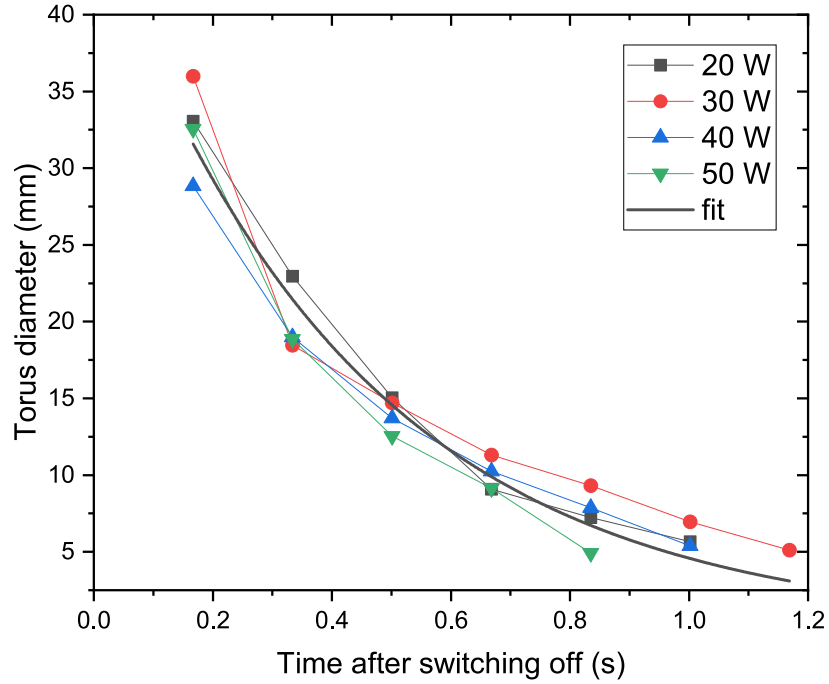
Figure 3.17: The graph of the torus diameter as a function of time for the experiments D. A fit to the concatenated data is displayed as well.

the plasma was switched off. From this number it can be concluded that it is very likely that the particles, which are responsible for the scattering, come from the plasma zone above the race track. Analogously, the parameter α describes the rate at which the cloud of nanoparticles shrinks.

The same procedure of evaluation was also done for the experiments C (corresponding to the lowest magnetron voltage) and for a comparison the data is plotted in figure 3.18. There are four graphs, each graph for a respective power, comparing the decay of the toroidal cloud after time point C and D. We see that the general behaviour is somewhat very similar, but the torus happens to decrease its size a bit slower for the situation when the plasma was switched off at the time point C. For a more precise determination, we fitted concatenated data for all experiments C with the exponential function defined by the equation 3.1 and obtained the fitting parameters:

$$
\begin{aligned}
d_0^C &= (45 \pm 4) \ \text{mm} \,, \\
\alpha^C &= (1,8 \pm 0,2) \ \text{s}^{-1} \,.
\end{aligned}
\tag{3.3}
$$

The initial torus diameter d_0^C is approximately of the same value as d_0^D for the experiments D, but the velocity parameter α^C is lower. This corresponds to the observation of a slower decrease in the torus diameter. The time point C precedes the time point D in the period and the particle growth. Thus, it is generally accepted that the mean particle size increases in the latter growth phases, so we expect that the formed particles in the time point D are bigger than those in the time point C. Hence, the size of the formed particles may play a role during shrinking of the nanoparticle cloud.

As already mentioned, while the discharge is running, there are number of forces acting on particles (electromagnetic, gravitational, ion drag, neutral drag,
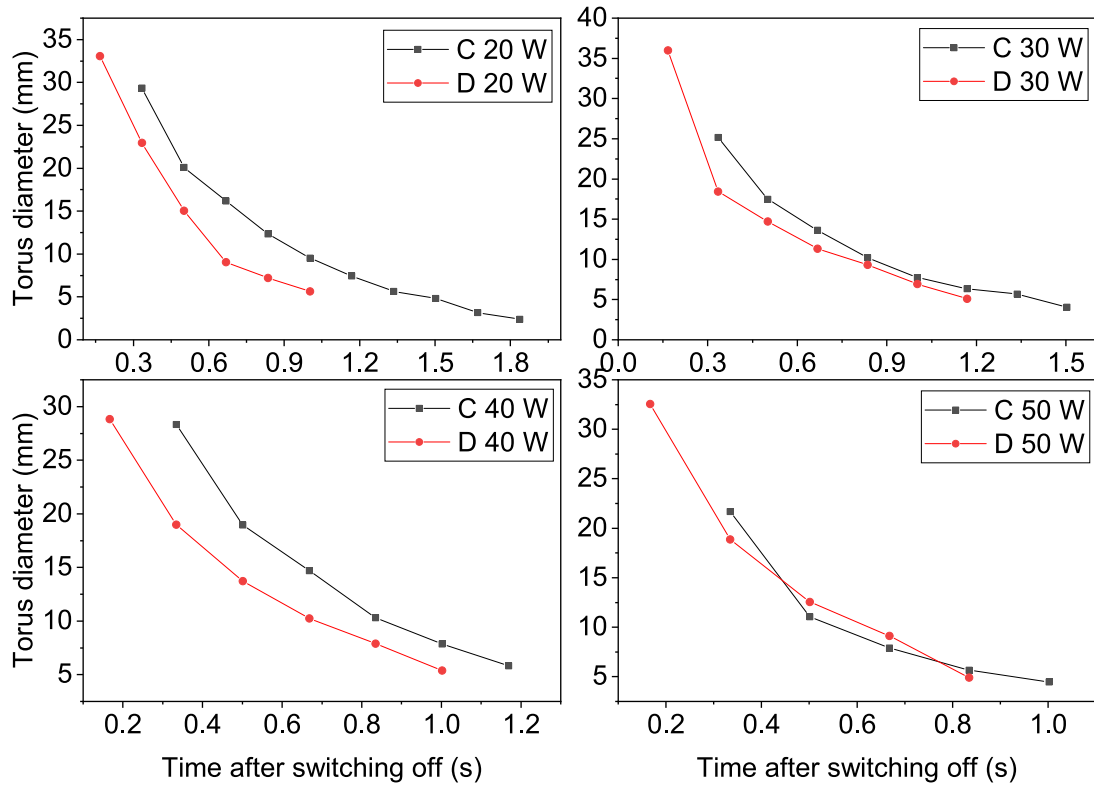
Figure 3.18: A set of graphs displaying the torus diameter versus time after turning off the the discharge. Data sets for four different power values are shown in four graphs, each graph comparing the torus decay at time point C and D (which correspond to latter phases of the particle growth).

thermophoretic, etc.). When the plasma ceases, some forces vanish immediately, others may disappear more gradually or even remain. We suggest that the neutral drag is the driving force of the process, because it is proportional to the cross section of the particles. Bigger particles possess bigger cross section and thus are also swept by the working gas easier. Nevertheless, for a clear conclusion further measurements are required.

In figure 3.18, the previous ideas does not seem to work for the case of 50 W. What needs to be taken into account here is that all the experiments were conducted manually (especially the turning off the discharge). Also, for 50 W the oscillation period is the shortest and the discharge is not very stable. These things together could cause the different decay behaviour for the experiment C with 50 W power. The very probable scenario is that the discharge was switched off, for example, one second later than the desired time point and at that time the discharge could already occur in the next phase of the period.

To conclude this part, the laser scattering experiments brought interesting results. Although some of them still need to be properly interpreted, which requires further highly focused experiments, the main outcome is the confirmation of the trapping of C:H:N:O nanoparticles in the aggregation chamber.

3.2 Silver deposition

The second experimental part was dedicated to the characterization of the inoculation zone, which is a part of the deposition setup where in-flight modification of C:H:N:O particles is meant to take place. The magnetron with nylon target was switched off for all the following experiments and only the magnetron with silver target was operated. The behavior of the discharge was studied with respect to pressure inside the inoculation chamber and magnetron current. In following paragraphs we describe the obtained results.
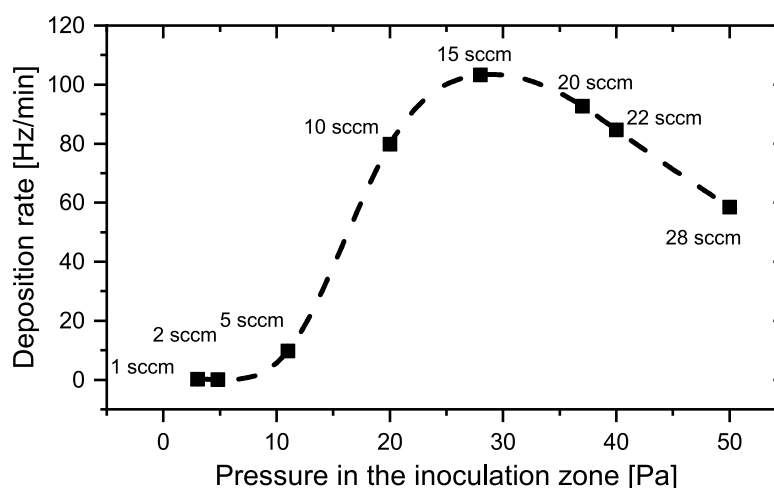
Figure 3.19: The deposition rate of silver in the deposition chamber as a function of pressure in the inoculation zone. The magnetron current of 100 mA was kept constant.

Firstly, we examined the aggregation properties of the inoculation zone. We measured the deposition rate in the deposition chamber by QCM and the pressure in the inoculation zone was varied up to 55 Pa. The results are displayed in figure 3.19. We observed very low deposition rate for low pressures as it is likely that no aggregation takes place and sputtered silver might come to chamber walls due to longer mean free path. As the pressure increases, the mean free path of the species is decreased and more collisions with the working gas happen, which helps to thermalize sputtered atoms. This promotes the condensation, formation of the nanoparticles and collimation of the nanoparticle beam towards the aperture. Such produced nanoparticles are then transported through the exit aperture into the main deposition chamber and are detected by QCM. The peak in the deposition rate is reached for approximately 30 Pa. Further rise of the pressure above this value is subsequently followed by a decrease in the deposition rate. In this pressure region, the clustering might become less efficient (e.g. because the collisions between silver species become less frequent), clusters can be scattered away or re-deposition on the target may become even more significant because of the shorter mean free path.

In the next step, we examined the deposition rate (QCM was again placed in the deposition chamber), but this time we varied the magnetron current. The gas
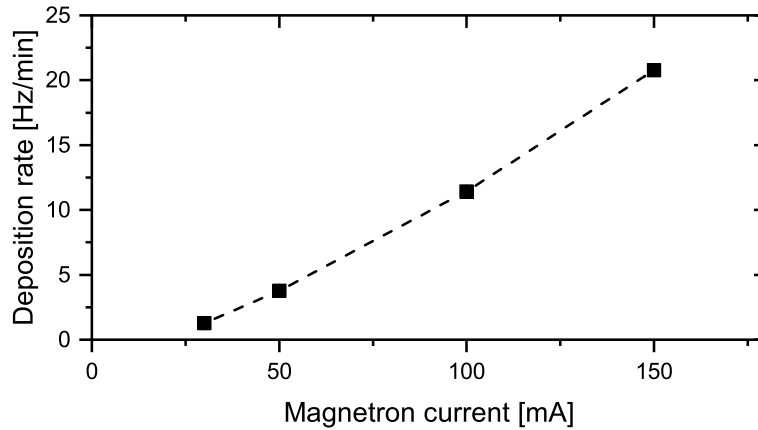
Figure 3.20: The deposition rate of silver in the deposition chamber as a function of magnetron current. The gas flow was 28 sccm and the pressure inside the inoculation chamber 55 Pa.

flow was kept at 28 sccm, which corresponds to 55 Pa in the inoculation zone. Obtained results evince a linear growth of the deposition rate with DC magnetron current as can be seen in figure 3.20.

Both previous results (figures 3.19 and 3.20) suggest that the inoculation zone behaves as a conventional gas aggregation source.
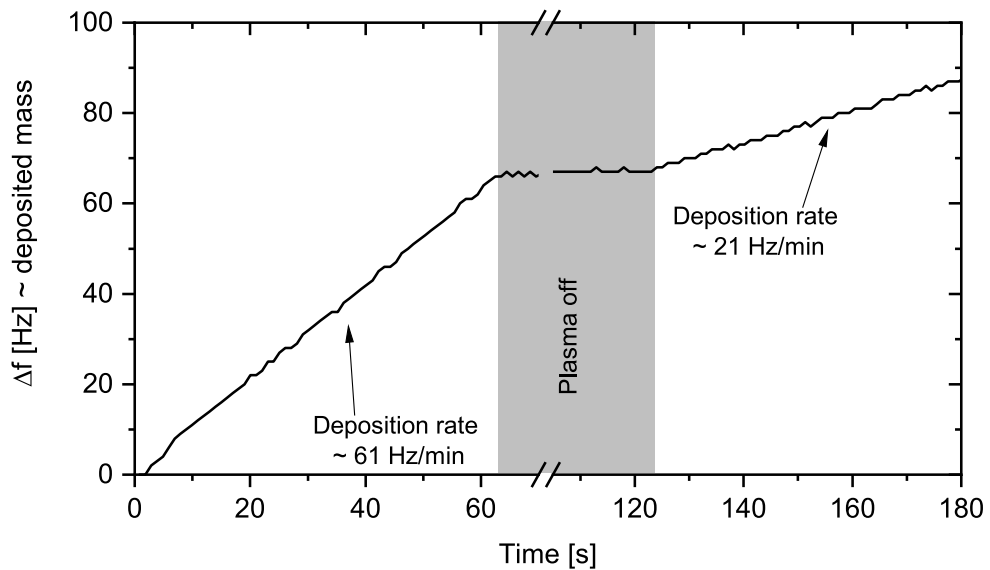
Figure 3.21: The deposited mass as a function of time measured in the deposition chamber. The DC magnetron in the inoculation was operated. The plasma was run for one minute, then it was switched off for another minute and meanwhile a substrate was inserted into the inoculation zone. During the last minute the discharge was operated again under the same conditions (55 Pa, 28 sccm, 100 mA) with the substrate in the inoculation chamber.

An additional experiment was carried out during which the deposition rate was monitored with respect to time. The whole experiment lasted three minutes in total and plasma was run during the initial and last minute. In the middle, the discharge was switched off and during this time a substrate (75 mm by 25 mm

glass slide) was inserted into the inoculation chamber. The results are presented in figure 3.21. We observed different deposition rates during the first and the last minute, although the same operating conditions were kept. This means that in the last third of the experiment the relatively significant fraction of sputtered material was not leaving the inoculation chamber in the form of Ag nanoparticles and was most likely deposited onto the inserted substrate.

Interestingly, we did not observe any periodic behavior as in the case of C:H:N:O nanoparticles. This finding does not mean that there are no oscillations at all. In fact, a recent article [77] reports that growth oscillations were observed during first few seconds of running magnetron discharge. The researchers used relatively similar magnetron-based gas aggregation cluster source and monitored the growth processes of silver nanoparticles inside their aggregation chamber with small angle X-ray scattering. Their investigation revealed that even though the oscillations cannot be detected by QCM, they are pronounced in terms of the average diameter and relative volume fraction of nanoparticles. One reason why these oscillation cannot be detected by QCM is its sampling frequency which might be insufficient for the observation of the frequency of oscillations. In their case, the growth frequency was of order of units of Hz, whereas our growth oscillations for C:H:N:O were the order of hundredths of Hz. Typically, the sampling frequency for the deposition rate measurement is in units of Hz. Therefore, it is possible that some growth induced instabilities might happen also in our inoculation zone, but we are not able to either confirm or disprove their presence with the datasets we acquired by available instruments.

To reveal some visual aspects of the silver particles collected in the main deposition chamber, specimens were prepared for TEM and SEM analysis. An example of acquired TEM image is in figure 3.22. The particles are round and exhibit a tendency to form larger aggregates, but the original spherical nanoparticles still remain well distinguishable. There are more options how these aggregates can be formed: nanoparticles can collide with each other still in the inoculation zone and undergo thus agglomeration by sintering, or they land on the substrate and next incoming nanoparticles can be attached to those already present on the substrate. Unlike the plasma polymer particles, metallic particles are much smaller and not so transparent for the electron beam.

An example of SEM image of produced nanoparticles is presented in figure 3.23. Similarly to the TEM image, the nanoparticles have spherical shape and exhibit a tendency to agglomerate. Single particles are rather rare and they prefer to be attached to each other. The statistical evaluation of nanoparticle sizes was done and is presented in figure 3.24. The mean value was (20 ± 7) nm, which means they are significantly smaller compared to C:H:N:O nanoparticles.

In order to investigate the possible formation of a deposit inside the inoculation zone of the experimental set-up, one silicon substrate was placed directly into the inoculation zone (facing the magnetron).

In figure 3.25, a SEM image of such a sample is displayed. In this case, small islands are formed on the interface with the substrate instead of spherical nanoparticles that were observed in the main deposition chamber. This indicates different growth mechanism of silver nanostructures deposited inside and outside the inoculation zone. When a substrate is inserted into the inoculation zone, atomic material can arrive to its surface and can start to condensate over there.
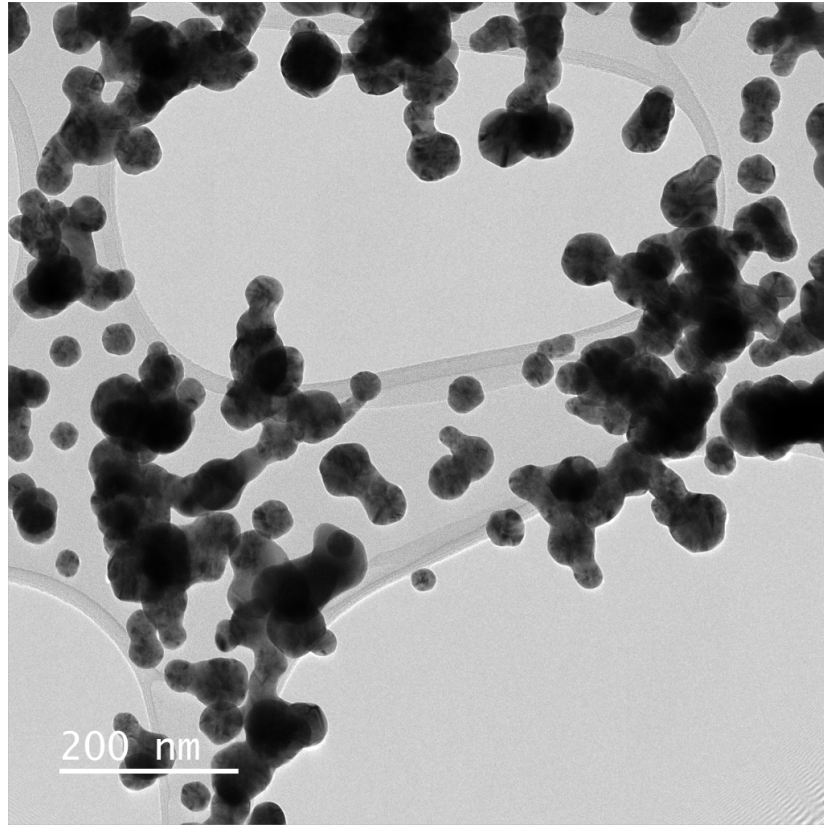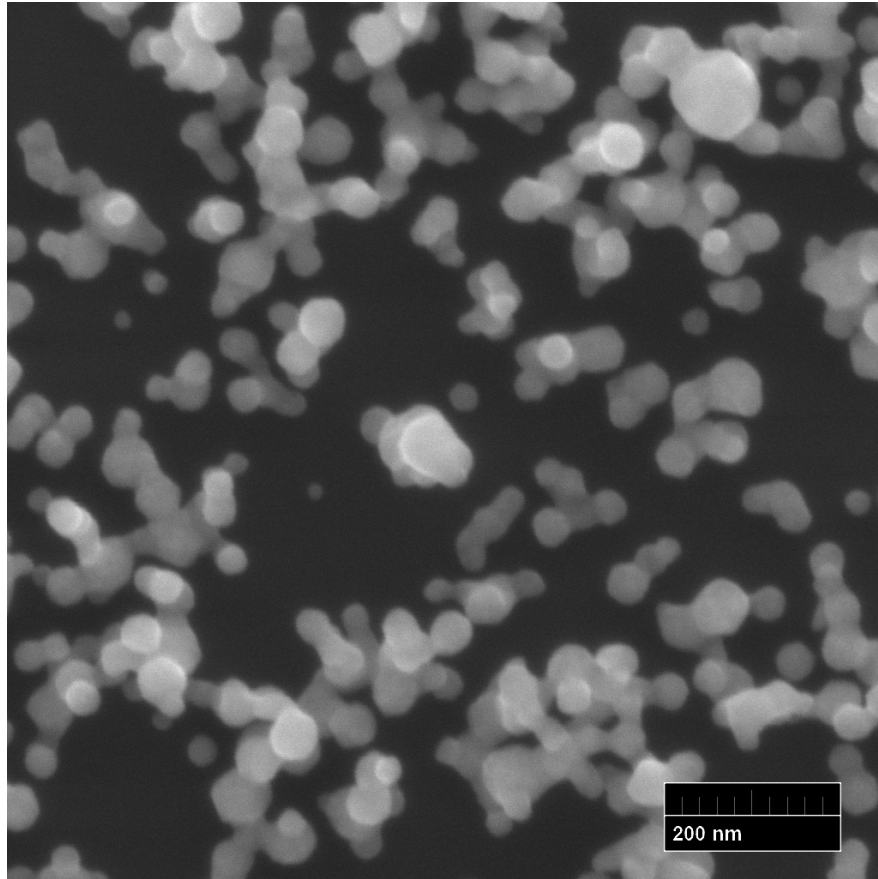
Figure 3.22: The TEM image of silver nanoparticles deposited on a TEM grid placed in the deposition chamber. Operating conditions in the inoculation zone were 55 Pa, 28 sccm, 100 mA.

Dimers and trimers can be formed (e.g. by surface diffusion) serving as nucleation sites for thin film formation. As more atoms join these sites, islands happen to grow and when they eventually grow big enough, a continuous thin film can be formed. This is a bit different nucleation mechanism than that of nanoparticles, because the nucleation occurs on a surface and not in the plasma volume. As we have seen the change in the deposition rate in figure 3.21, when a substrate is inserted into the inoculation zone, the deposition rate in the adjacent chamber decreases. We expect that the amount of sputtered material remained the same, but somehow the material preferred to stay inside the inoculation zone when additional substrate was present. The reason for this might be that silver prefers nucleation on surfaces than in the plasma volume. For creation of nucleation sites in the plasma volume, three-body collisions are usually needed. A very naive idea is that the substrate can actually serve as the needed third body in a collision on its surface for stabilizing a dimer and thus creating a nucleation site. Hence, the probability of creating a nucleation site on the surface of a substrate can be higher than that of in the bulk plasma. Such phenomenon is also consistent with observed decrease of the deposition rate of Ag nanoparticles in the main deposition chamber when a solid substrate was introduced into the inoculation zone (see 3.21.)

Another set of samples was prepared for the same operating conditions in the inoculation zone, but soda lime glass instead of silicon was used as a substrate this time. These specimens prepared in the deposition chamber and in the inoculation
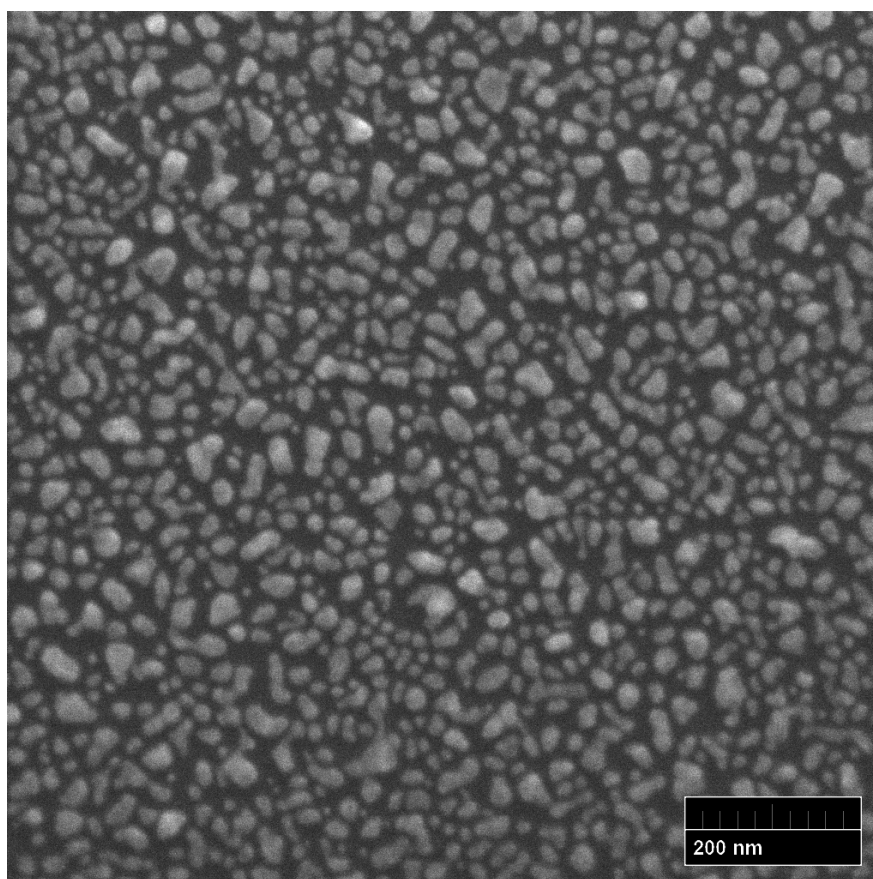
Figure 3.23: The SEM image of silver nanoparticles deposited on a silicon substrate placed in the deposition chamber. Operating conditions in the inoculation zone were 55 Pa, 28 sccm and DC magnetron current 100 mA, deposition time 5 min.

zone were examined by UV-Vis spectrometry and results can be found in figures 3.26 and 3.27 respectively.

In figure 3.26, absorbance of silver nanoparticle film deposited in the main deposition chamber is plotted as a function of wavelength. The deposition time was varied from 0.5 min to 20 min. For short deposition times, the absorbance is almost negligible, but clearly with longer deposition times a LSPR peak appears at approximately 360 nm. This peak seems to stay at the same wavelength, which means no redshift is present, and grows in intensity for longer deposition times. We expect that for longer deposition times, more material is present in the final sample. Therefore, the increasing intensity is reflecting the amount of Ag particles present on the specimen. Moreover, LSPR signal reflects the characteristic sizes and shapes of the silver nanostructures. At the same time, we assume that once nanoparticles leave the inoculation zone (which provides their aggregation), their formation and growth is terminated. With constant flow of working gas and constant deposition rate over time, prolonging the deposition time is thus not increasing the size of the nanoparticles that leave the aggregating zone, but it changes only their amount on the sample. Because the size distribution stays the same over the whole deposition procedure, the LSPR peak does not experience any shift in its position. We can also notice a smaller second bump between
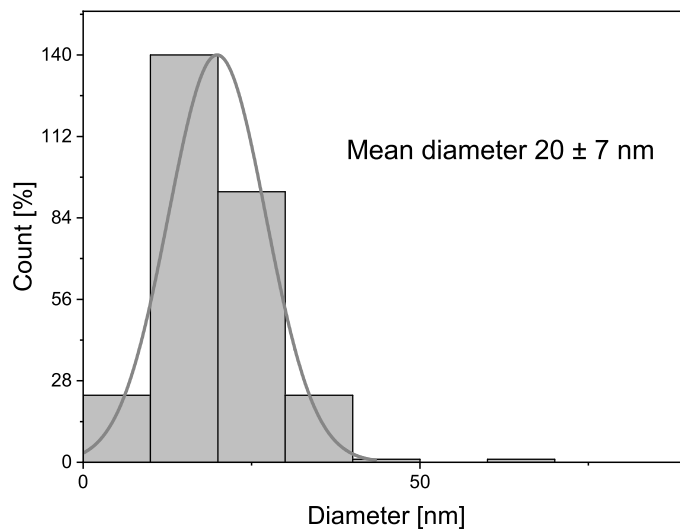
Figure 3.24: The size distribution of silver nanoparticles formed at the DC current of 100 mA. The mean diameter is (20 ± 7) nm. Other operating conditions in the inoculation zone were 55 Pa, 28 sccm.

Figure 3.25: SEM image of silver islands deposited a silicon substrate placed in the inoculation chamber. Operating conditions in the inoculation zone were 55 Pa, 28 sccm, 100 mA and deposition time 15 s.
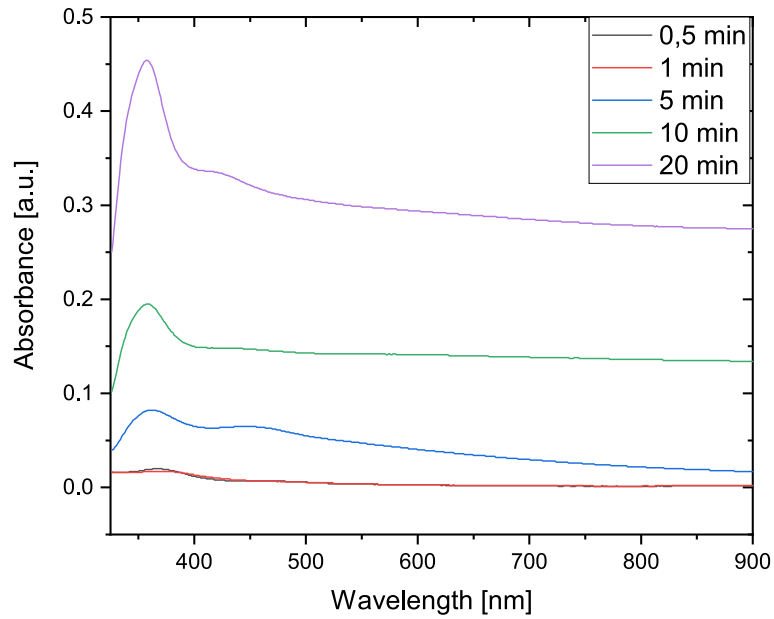
Figure 3.26: UV-Vis spectra of silver nanoparticles deposited on soda lime glass in the deposition chamber. The deposition time was ranged from 0.5 min to 20 min. Other operating conditions were 55 Pa, 28 sccm, 100 mA.

400 nm and 500 nm, which also does not seem to change its position. In the TEM and SEM images, we saw that nanoparticles form bigger aggregates. Thus the second smaller bump can be assigned to the characteristic size of these bigger objects.
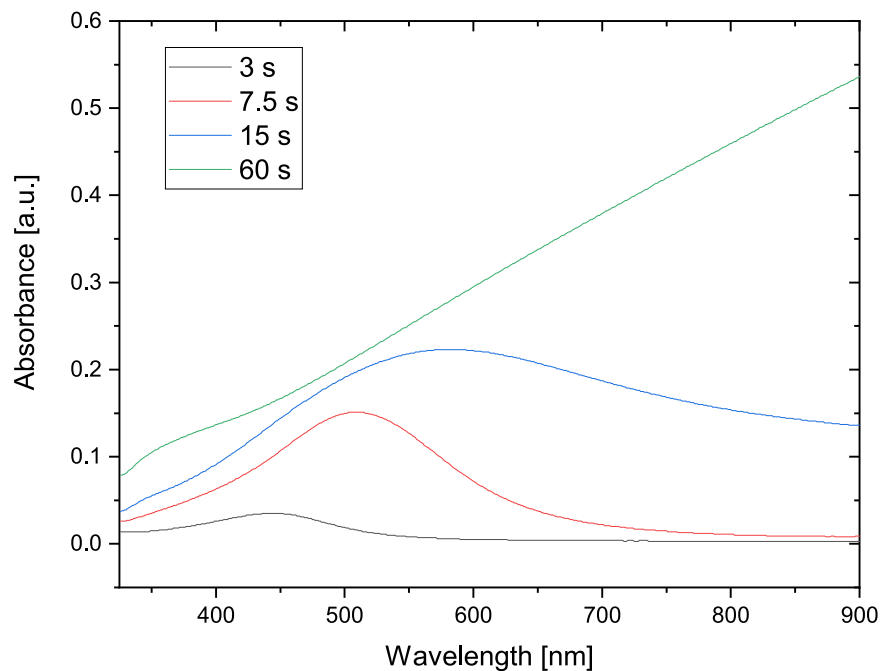
Figure 3.27: UV-Vis spectra of silver deposited on soda lime glass in the inoculation chamber. The deposition time was ranged from 3 s to 60 s. Other operating conditions were 55 Pa, 28 sccm, 100 mA.

The second set of samples for UV-Vis analysis was prepared under the same

operating conditions, only the deposition time ranged from 3 s to 60 s. This time the samples were placed in the inoculation zone during the deposition process. Results of UV-Vis measurement can be found in figure 3.27. Markedly different optical properties of such prepared samples were observed as compared to the samples deposited in the main deposition chamber. For the shortest deposition time, the absorbance is very low yet LSPR peak is detected. With longer deposition times the red shift and broadening of the peak is observed and, finally, the longest deposition rate led to monotonous growth of absorbance with respect to wavelength. Similar results were already reported in the literature for magnetron sputtered silver and may be explained by nano-island growth mechanism. [20] As already mentioned, the position of the peak is connected to the size of the silver nanostructures and distances between them. Shifting of the peak towards longer wavelengths is indicating the growth of the Ag islands as well as decrease of the distances between them that causes increased electromagnetic coupling between them. Broadening of the peak is related to coalescence of the growing nano-islands and formation of worm like structure. Vanishing of the LSPR peak for the longest deposition time is pointing to the change from the island structure to an interconnected thin film with metallic properties.

To conclude this part, we have demonstrated that the inoculation zone, when no C:H:N:O particles fly through it, behaves as a conventional gas aggregation source of metallic nanoparticles. However, it is also shown that clustering is disturbed by the presence of a solid substrate. In this situation, the significant fraction of sputtered atoms condenses on such a substrate where the condensing atoms form nano-islands that grow in size with increasing deposition time. This phenomenon competes with the volume nucleation of silver and lowers thus overall production of Ag nanoparticles that leave the inoculation part of the deposition system.

3.3 Heterogeneous silver-plasma polymer nanoparticles

This section is dedicated to the actual preparation of the heterogeneous nanoparticles. Previous two sub-chapters were investigating the preparation of nanoparticles for each part of the experimental setup separately. Here, we combine both of them and study the properties of the resulting nanomaterial.

For the preparation of the core nanoparticles, the operating conditions were chosen as follows: RF magnetron power 40 W, Ar gas flow 28 sccm, pressure in plasma polymer GAS chamber 122 Pa, pressure in the inoculation zone 55 Pa, pressure in the deposition chamber 5 Pa. The DC current on magnetron with silver target was varied up to 300 mA.
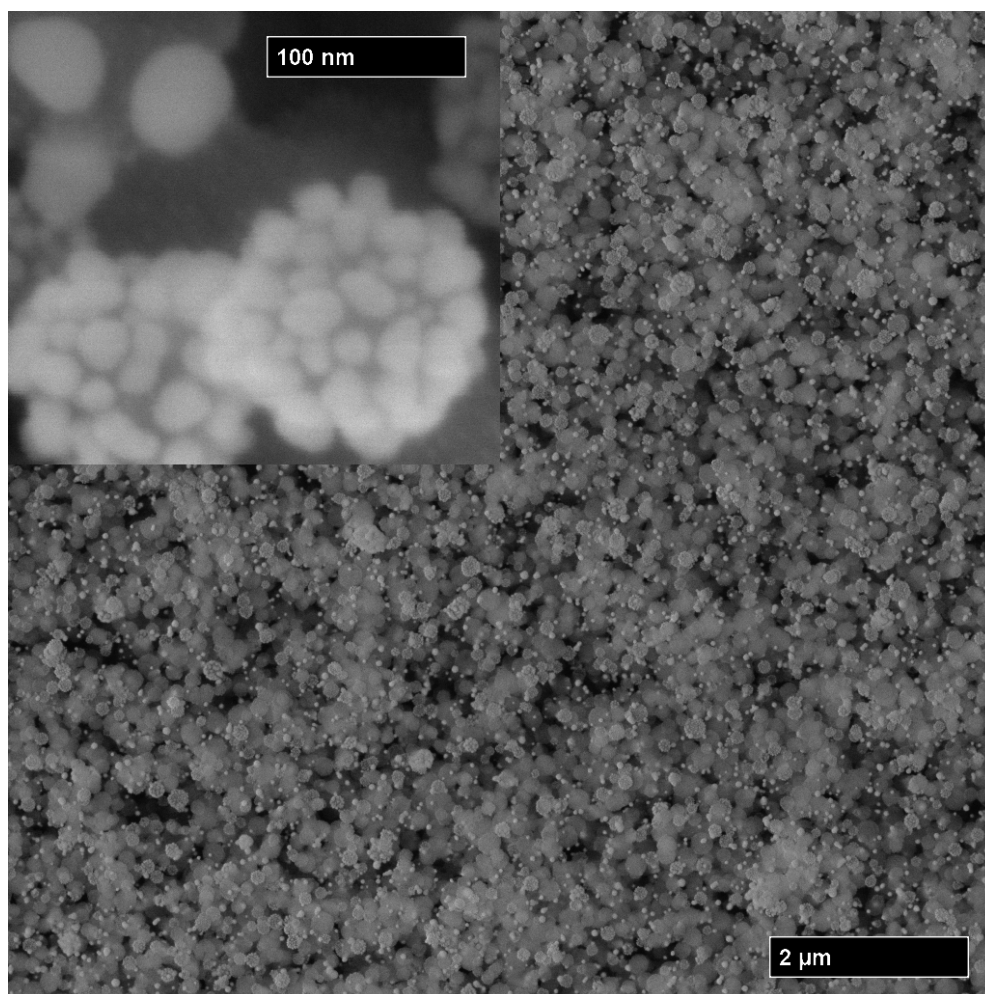
Figure 3.28: The SEM image of the deposited nanoparticles when both magnetrons are operated. RF power 40 W, DC current 100 mA, Ar flow 28 sccm.

For SEM investigation we prepared a sample on a silicon substrate under conditions described in the previous lines and DC magnetron current 100 mA. An example of SEM image of deposited nanoparticles is displayed in figure 3.28. The morphology of the nanoparticles is markedly different from that one of bare C:H:N:O nanoparticles (compare with figure 3.7). The particles appear much rougher as the core particles are now modified by the active inoculation zone

that leads to the formation of small metallic satellites attached to C:H:N:O core. On the other hand, we also observe free-standing Ag particles, i.e. nanoparticles that are not attached onto plasma polymer cores. The reason for this is following. From the previous experiments we know that plasma polymer particles leave the aggregation chamber at well-defined time intervals and for the rest of the time, the amount of material coming from this part of setup is negligible. On the contrary, the inoculation zone does not exhibit such temporal instability, but the deposition rate is rather affected by presence of an additional substrate inside the inoculation zone. We suggest that C:H:N:O particles can serve as such substrates during the time they fly through the inoculation zone. However, for the rest of the time, the silver nanoparticles are not hindered from formation and thus such nanoparticles may reach a substrate located in the main deposition chamber. The diameters of these particles also roughly correspond to those of pure silver prepared when the nylon magnetron was switched off (compare with figure 3.23).
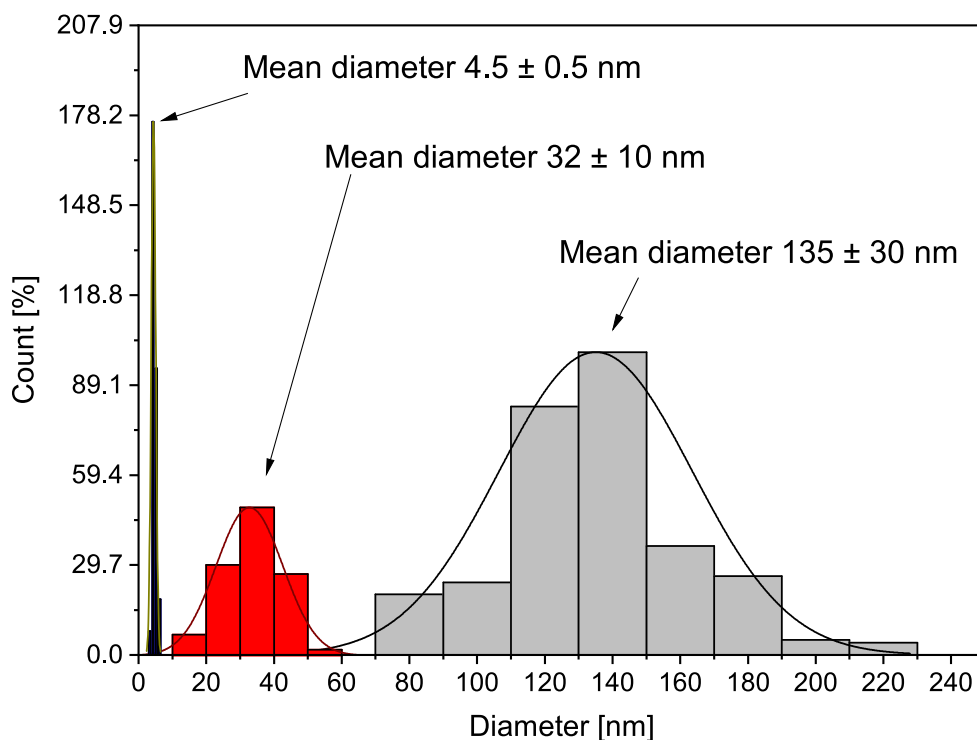
Figure 3.29: The size distribution of heterogeneous particles, their satellites and free-standing nanoparticles. Prepared under following conditions: RF power 40 W, DC current 100 mA, Ar flow 28 sccm.

The statistical analysis of SEM images was performed and we estimated the mean diameter of heterogeneous nanoparticles as well as of the satellites and free-standing nanoparticles. The resulting histograms can be found in figure 3.29. From the Gaussian fit, it follows that the mean diameter of the core-satellite particles was (135 ± 30) nm, for the satellites only (4.5 ± 0.5) nm and for the free-standing nanoparticles (32 ± 10) nm. The size of whole particles is comparable to that one of bare C:H:N:O particles. This proves that after the core particles are formed and leave the gas aggregation source, the inoculation process does not affect their sizes much. On the other hand, the presence of plasma polymer particles in the inoculation zone does affect the silver aggregation. The

(a) 0 mA - a bare C:H:N:O particle   (b) 50 mA

(c) 100 mA   (d) 150 mA
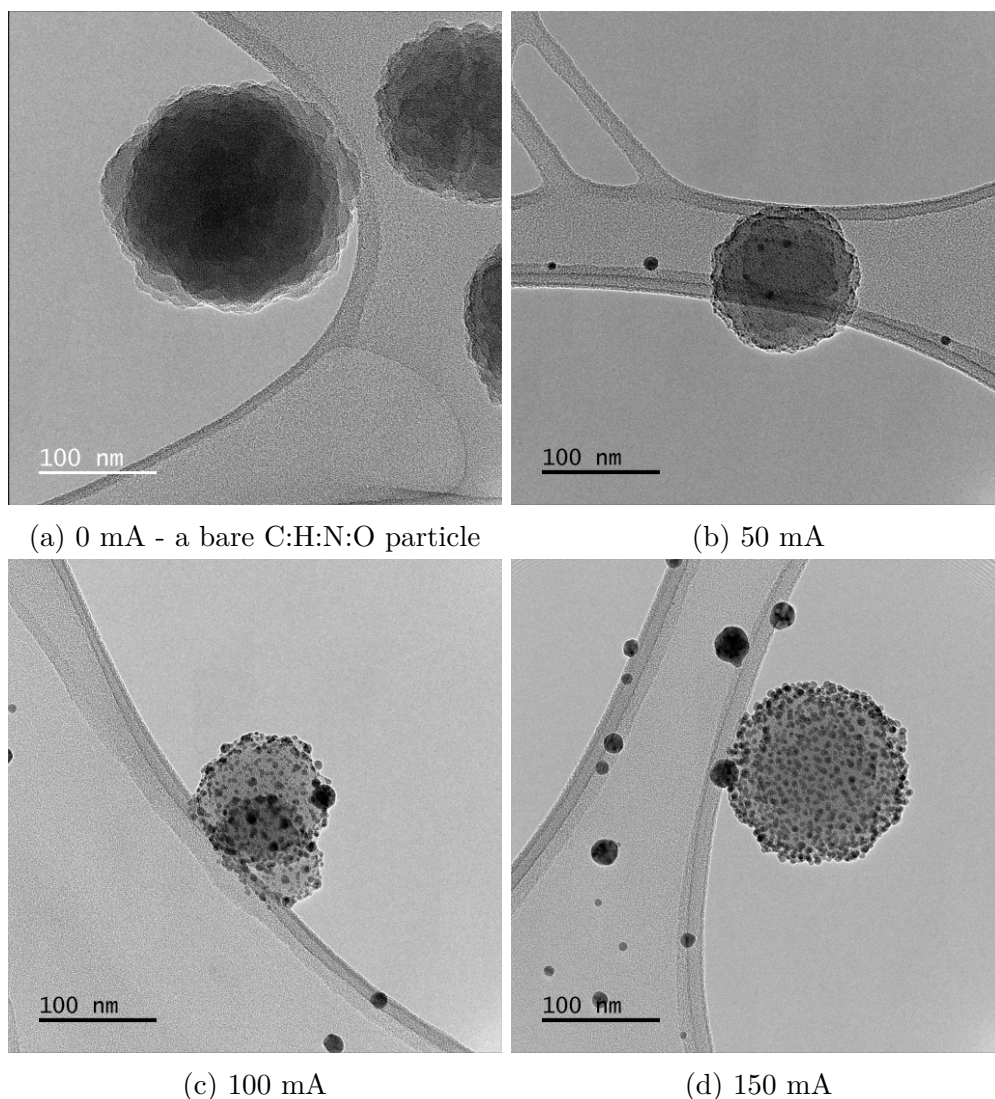
Figure 3.30: TEM images of core-satellite nanoparticles. The core material is C:H:N:O plasma polymer, the satellites are made of silver. Operating conditions were RF power 40 W, Ar flow 28 sccm and DC current is written in the caption of the particular inset.

mean size of the silver nanoparticles decreases greatly when they appear in the form of satellites. It is very likely that these silver satellites are actually islands created during the early stages of thin film formation in a similar manner as observed when a solid substrate was introduced into the inoculation zone during the formation of Ag nanoparticles. Furthermore, as the C:H:N:O particles do not stay in the inoculation zone long enough (an estimated residence time of C:H:N:O nanoparticles in the inoculation zone is in the order of seconds) they are not covered entirely by silver. Therefore, a continuous metallic shell is not formed on the surface of plasma polymer particles. Furthermore, the mean diameter of free-standing (silver) nanoparticles is comparable to the case when only the inoculation zone was active and no C:H:N:O particles were produced (see figure 3.24).

To capture even more structural details of prepared particles as well as to test the possibility to control the size and number of Ag satellites on C:H:N:O

cores, four specimens were readied for TEM analysis. The RF power and argon flow was 40 W and 28 sccm respectively. The DC current on the magnetron with silver target was different for each specimen with values of 0 mA (bare C:H:N:O nanoparticles), 50 mA, 100 mA, 150 mA and 300 mA. The examples of taken TEM images are displayed in figure 3.30. For the very low DC current (see figure 3.30b), the heterogeneous particle looks very similar to that one of bare C:H:N:O plasma polymer (see figure 3.30a). It is very likely that there is not enough of sputtered material to modify the surface of the particles flying through the inoculation zone. As the current rises, we observe that the particles get more satellites and these satellites also increase in their size. This is connected with the higher amount of silver released from the sputtering target at higher DC magnetron currents that enhances the fluence of silver to C:H:N:O cores and speeds up the silver nano-island growth. But not only that happens. At the same time, we see the increase of the number of free-standing silver particles, which is most likely the result of periodic release of the plasma polymer particles and higher production of Ag nanoparticles at higher magnetron currents when no C:H:N:O particles are present in the inoculation zone (see figure 3.20).
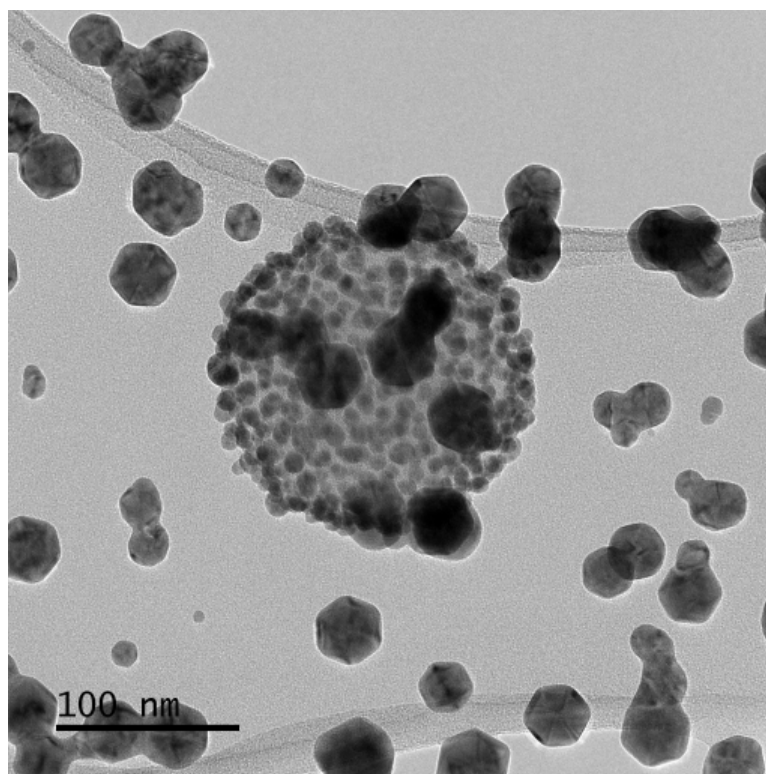
Figure 3.31: The TEM image of the core-satellite particles for RF power 40 W, Ar flow 28 sccm and DC current 300 mA. The core material is C:H:N:O plasma polymer, the satellites are made of silver.

The occurrence of free-standing Ag nanoparticles is especially pronounced for very high DC current. In figure 3.31 (an example of a TEM image), the DC current was 300 mA and the free-standing silver nanoparticles are not rare anymore and their amount largely exceeds the number of heterogeneous Ag/C:H:N:O core-satellite particles. Because of this, the deposits produced in such a way exhibit properties that are nearer to the properties of homogeneous silver nanoparticle

films. For this reason we did not investigate further the properties of such samples. On the other hand, this technological problem that is connected with the self-pulsing of the release of C:H:N:O nanoparticles could be overcome. For example, the inoculation zone could be synchronized with the C:H:N:O particle bursts in such a way that the inoculation zone could be active (the magnetron inside is switched on) only while the plasma polymer particles are present in this region. The second possible option involves the mass filtration of nanoparticles before they reach the substrate. These kinds of experiments are left for further investigation elsewhere.
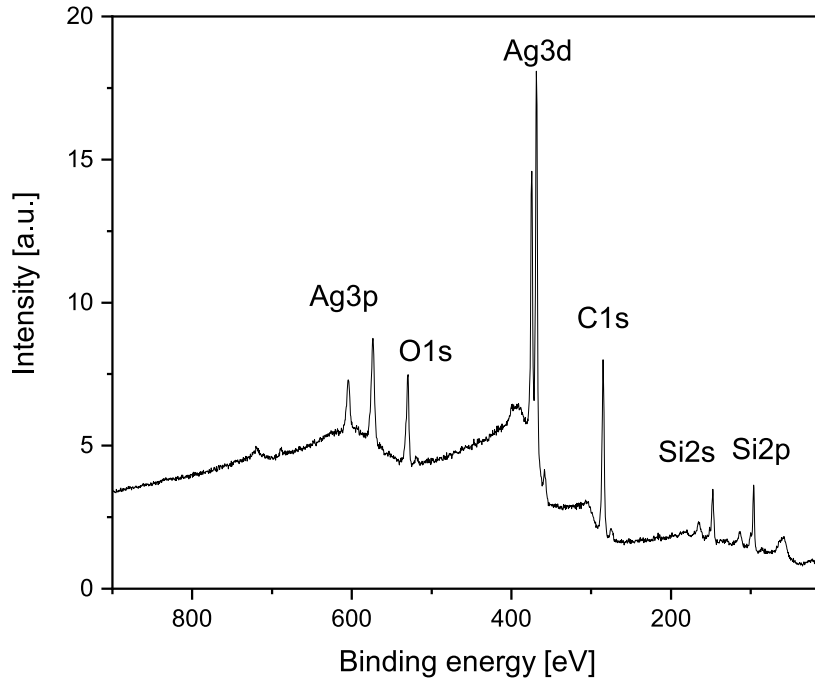
Figure 3.32: The survey spectrum of the deposited particles from XPS measurement. The deposition was done under following conditions: RF power 40 W, DC current 100 mA, Ar flow 28 sccm.

DC current [mA]	C [at.%]	N [at.%]	O [at.%]	Si [at.%]	Ag [at.%]	Ag/C [rel.]
0	40.0	1.7	15.4	42.9	0.0	0.00
50	16.0	0.6	21.3	61.9	0.3	0.02
100	17.0	1.3	19.8	60.9	1.0	0.06
150	16.6	2.2	21.7	53.2	6.3	0.38

Table 3.1: Elemental composition of heterogeneous nanoparticles using different DC current on the magnetron with silver target.

Besides morphology, also chemical structure and optical properties of produced core-satellite nanoparticles were evaluated in this study. The chemical

analysis was done by XPS and an example of survey spectra is shown in figure 3.32. Additionally to the peaks from C:H:N:O particles and the silicon substrates (compare with figure 3.32), other peaks that can be assigned to silver were also detected in the XPS spectra. The quantitative analysis of the XPS spectra revealed how the chemical composition changes with the DC magnetron current. The results are presented in table 3.1. For example, the content of silver (and similarly Ag/C ratio) rises monotonously with DC magnetron current. This might be a logical consequence, because with higher DC currents the sputtering of silver target becomes more efficient and thus more silver material can be transported to the substrate in the deposition chamber either in the form of small satellites on C:H:N:O cores or as free-standing Ag nanoparticles.
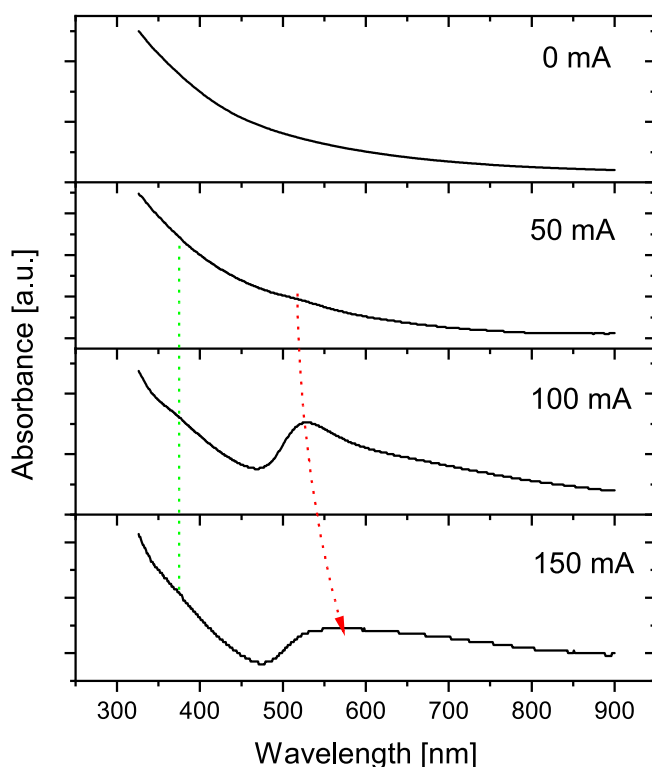
Figure 3.33: UV-vis spectra of heterogeneous nanoparticles for different DC magnetron currents.

The optical properties of the core-satellite particles were examined by UV-Vis spectrometry. The absorption spectra are displayed in figure 3.33. With increasing DC current the LSPR peak of silver grows and shifts its position towards the longer wavelengths. These results show some similarities to what we already observed for silver islands that were formed on a substrate introduced into the inoculation zone that points on the nano-island growth mechanism of Ag satellites. As already mentioned, the wavelength of the LSPR peak is connected with the characteristic size of the probed objects. Therefore, the redshift of the LSPR peak indicates the change of the mean size of the objects, particularly their growth. Broadening of the LSPR peak then points to the "width" of the size distribution of the satellites and the interaction between them. The reasoning is pretty much the same as the one for silver islands, the difference is that the structure in the specimen is not in plane, but rather a 3D structure, so the

inter-satellite interactions can become more significant for thicker deposits. For higher DC currents, the mean diameter of the satellites and also their amount grow and correspondingly, the LSPR peak becomes more prominent. Additionally, there are also other factors that affect the absorption peak, e.g. shape of the satellites and permittivity of the environment. Even though the shape of the satellites appears round, it is questionable whether the shape is spherical or more flat and circular only. Furthermore, C:H:N:O plasma polymer differs in permittivity from air or silicon. These two factors also affect the position and the shape of the LSPR peak that may be thus a bit red-shifted in comparison to what would be observed on glass used as an substrate. Finally, it is worth noting that at wavelength of approximately 360 nm we observe a gentle build-up of a shoulder with increasing DC power that is shadowed by C:H:N:O plasma polymer absorption. This signal can be attributed to free-standing silver nanoparticles as we expect them to have similar properties as in case of only silver nanoparticles (compare with figure 3.26).

3.4 Other materials

On the previous pages, we proved that it is possible to produce heterogeneous core-satellite nanoparticles made of sputtered nylon and silver through vacuum-based technique. As other combinations of materials can be interesting for various applications, we also performed preliminary tests to explore the versatility of this deposition strategy. In these experiments, we exchanged the target on the magnetron in the inoculation zone.
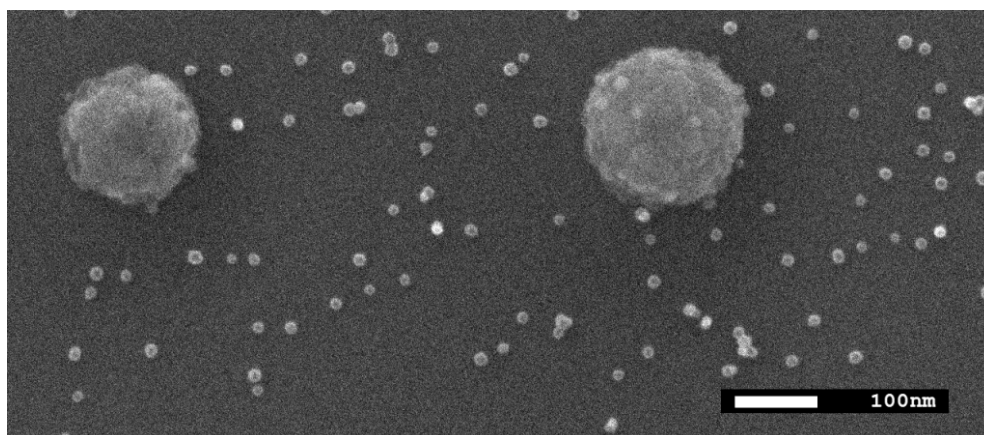
(a) 100 mA
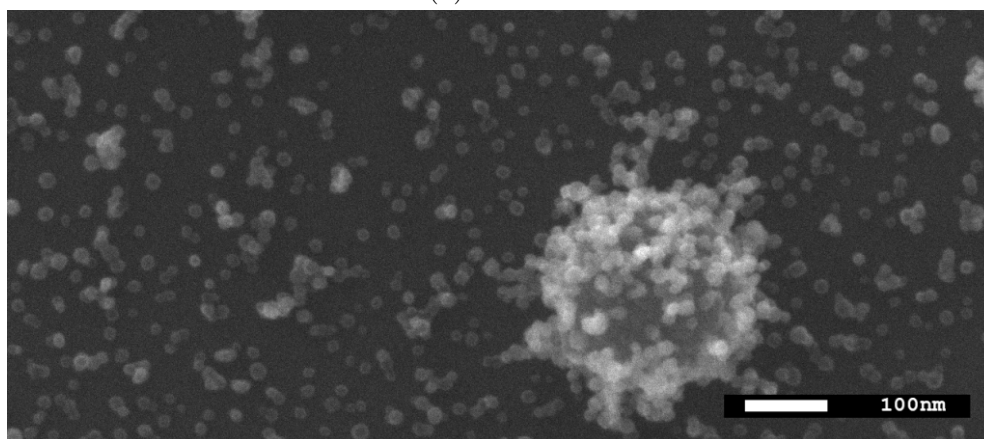
(b) 200 mA

Figure 3.34: The SEM image of the deposited nanoparticles when both magnetrons are operated. The magnetron in the inoculation zone was equipped with titanium target. RF power 40 W, and Ar flow 28 sccm. DC current is written in the caption of the particular inset.

First material we tried was titanium. It is a transition metal with high strength-to-weight ratio that is used in many applications (e.g. automotive, biomedical, dental, aerospace, etc.). Especially its non-toxicity makes titanium very interesting for wider use in the medical field.

The plasma polymer particles were produced as usual with RF power 40 W and argon flow 28 sccm. The magnetron in the inoculation zone was equipped with titanium target and operated with DC current 100 mA, so operating conditions were comparable to those when silver was used. We prepared a sample for SEM analysis and an example of such acquired image is shown in figure 3.34a.

Although we see a certain amount of free-standing Ti nanoparticles with diameters significantly smaller than that of C:H:N:O particles, the cores do not seem to be much modified and the inoculation process might not be effective. This may be caused by insufficient amount of Ti available for coating of the plasma polymer nanoparticles. At this point it is worth mentioning that Ti has much lower sputter yield as compared to silver.

For this reason, we prepared another sample in the same manner, but we increased the DC magnetron current in the inoculation zone to 200 mA, an example of a SEM image is displayed in figure 3.34b. Consequently, the amount of free-standing titanium nanoparticles rises and they also appear bigger. On the other hand, it seems like the titanium nanoparticles are a bit more concentrated on the plasma polymer core in this case, which could point to successful inoculation process. But unlike in case of silver, it appears that the free-standing nanoparticles and satellites do not differ in size at a glance. This could mean that the inoculation is underlain by a different mechanism. For instance, a possible explanation could be that titanium nanoparticles are being formed regardless of presence of an additional substrate (in other words the nucleation process in volume is favoured) and afterwards they can get attached to the plasma polymer particles or simply leave the inoculation zone and be deposited on a substrate.
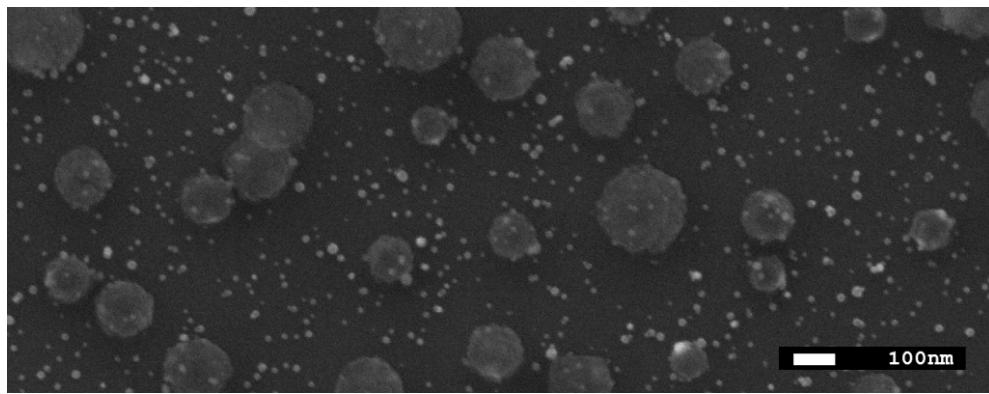
(a) 100 mA
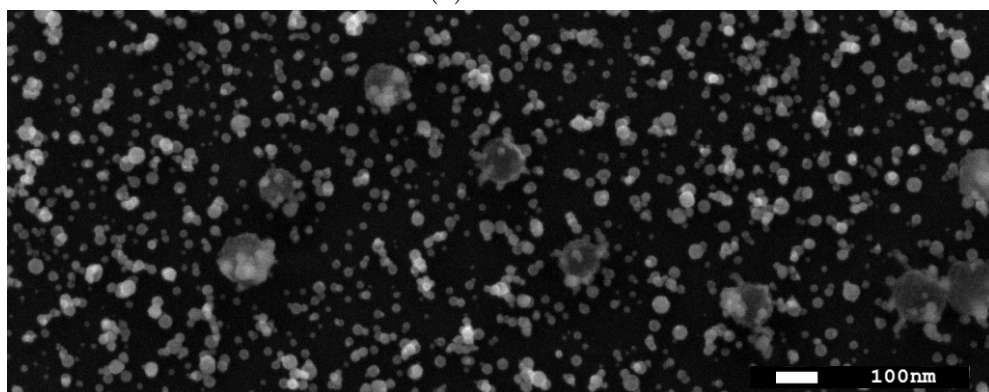
(b) 200 mA

Figure 3.35: The SEM image of the deposited nanoparticles when both magnetrons are operated. The magnetron in the inoculation zone was equipped with copper target. RF power 40 W, and Ar flow 28 sccm. DC current is written in the caption of the particular inset.

For another set of experiments, a copper target was used in the inoculation zone. Copper is especially known for its exceptional electrical conductivity, but it is also used when antimicrobial properties are needed.

The operating conditions were analogous to that one with titanium and silver, which means: RF power 40 W, Ar flow 28 sccm, DC current 100 mA. An example SEM image prepared in the same manner as in the previous experiments is displayed in figure 3.35a. The formation of free-standing copper nanoparticles is evident. Again, it does not seem that satellites are formed much, although some smaller nanoparticles appear on the C:H:N:O particles.

Similarly to titanium experiments, we increased the DC current to 200 mA and prepared a sample for SEM analysis, an example of it is presented in figure 3.35b. We see a certain number of smaller nanoparticles on plasma polymer cores. Similarly to titanium experiments, the nanoparticles on the C:H:N:O particles and the free-standing nanoparticles do not seem to differ much in size. It looks like that copper nanoparticles are homogeneously spread over the whole sample, which can be explained by two hypotheses. Both, the C:H:N:O and copper nanoparticles, could fly to the substrate independently or an in-flight modification of the C:H:N:O core particles could happen in the inoculation zone. In this case, the SEM image does not provide us much information about whether the inoculation process is successful or not and thus we cannot decide which hypothesis is more probable.

Even though the preliminary experiments look promising especially in case of titanium, a further investigation is needed to fully understand the inoculation process and its governing factors. Moreover, based on these experiments it seems that for some materials the inoculation process might be based on different mechanism from island growth as we observed in case of silver.

Conclusion

This thesis focused on production of heterogeneous metal/plasma polymer nano-particles through purely physical approach. The experimental setup consisted of two separate aggregation chambers and a deposition chamber. In the first aggregation chamber, plasma polymer particles were formed. Then these particles entered the second aggregation chamber (in other words the inoculation chamber) where the in-flight modification of those particles was taking place. The result of this in-flight modification was the formation of metallic satellites on plasma polymer cores and such particles travelled into the deposition chamber, where they were collected on substrates.

The work focused on several important topics of this fabrication strategy:

1) production of C:H:N:O particles;
2) silver deposition and formation of nanoparticles;
3) evaluation of properties of produced core-satellite nanoparticles and
4) testing the possibility to use the same approach for the production of satel-lites from other metals.

In the first part, we found out that the formation process of C:H:N:O particles follows a periodic behaviour known from the field of dusty plasma physics as *growth induced instabilities.* This causes a periodical release of nanoparticles from the aggregation chamber during limited time intervals. From the laser light scattering experiments, we discovered that these particles are very likely growing in the plasma zone above racetrack of the magnetron.

Next, we focused on the characterization of the second aggregation (or in other words inoculation) chamber with silver target mounted on the magnetron. Based on the acquired data, we concluded that this part of experimental setup behaves as a conventional gas aggregation source. On the other hand, when an additional substrate is present, silver readily nucleates on it.

The third experimental part was dedicated to characterization of the hetero-geneous core-satellite nanoparticles themselves. SEM and TEM analysis revealed that the formation of such particles is possible by our chosen route. Moreover, we showed that it is possible to control the size and the amount of silver satellites through adjusting the magnetron current in the inoculation zone. From our UV-Vis measurement, we conclude that it is possible to tailor the optical properties of these nanoparticles in this way. Nevertheless, the free-standing metallic particles were detected as well, which points to the weaknesses of this production process and is related to growth induced instabilities of the C:H:N:O particle production. Although no experiments were performed in this direction, we believe that the population of free-standing silver nanoparticles may be reduced. For example, the magnetron placed in the inoculation chamber can be synchronized with the periodic pulses of released C:H:N:O particles or, eventually, the particles can pass through an additional mass/size filter before they reach the substrate.

In the last section, we tried to produce satellites out of two other materials (titanium and copper). The preliminary results show that the inoculation process might be driven by other factors than those of silver. In case of silver, we expect that the satellites are formed on the core particles through island growth. This

might not be the case for titanium satellites. In case of copper, further investigation is needed to rule out whether the inoculation took place under chosen conditions.

To conclude, a novel approach to production of heterogeneous core-satellite metal-plasma polymer nanoparticles was introduced in this thesis. The deposition process was described in detail and characterized for the combination of sputtered nylon and silver. Furthermore, the preliminary experiments with other metals show promising results, so it might be possible to produce this type of two-component particles out of variety of materials. Most of the obtained results were also published in the literature. [61, 78, 79] On the other hand, more detailed studies are still needed for better understanding of the inoculation process.

Bibliography

[1] H. Haberland, M. Karrais, and M. Mall. A new type of cluster-ion source for thin film deposition. *MRS Proceedings*, 206, 1990.

[2] T. Hihara and K. Sumiyama. Formation and size control of a ni cluster by plasma gas condensation. *Journal of Applied Physics*, 84(9):5270–5276, nov 1998.

[3] S. Yamamuro, K. Sumiyama, and K. Suzuki. Monodispersed cr cluster formation by plasma-gas-condensation. *Journal of Applied Physics*, 85(1):483–489, jan 1999.

[4] S. Pratontep, S. J. Carroll, C. Xirouchaki, M. Streun, and R. E. Palmer. Size-selected cluster beam source based on radio frequency magnetron plasma sputtering and gas condensation. *Review of Scientific Instruments*, 76(4):045103, apr 2005.

[5] C. M. Wang, D. R. Baer, J. E. Amonette, M. H. Engelhard, Y. Qiang, and J. Antony. Morphology and oxide shell structure of iron nanoparticles grown by sputter-gas-aggregation. *Nanotechnology*, 18(25):255603, may 2007.

[6] Y.-H. Xu and J.-P. Wang. Direct gas-phase synthesis of heterostructured nanoparticles through phase separation and surface segregation. *Advanced Materials*, 20(5):994–999, mar 2008.

[7] D. Llamosa, M. Ruano, L. Martínez, A. Mayoral, E. Roman, M. García-Hernández, and Y. Huttel. The ultimate step towards a tailored engineering of core@shell and core@shell@shell nanoparticles. *Nanoscale*, 6(22):13483–13486, 2014.

[8] H. Kobayashi, A. T. Bell, and M. Shen. Formation of an amorphous powder during the polymerization of ethylene in a radio-frequency discharge. *Journal of Applied Polymer Science*, 17(3):885–892, mar 1973.

[9] O. Polonskyi, O. Kylián, P. Solař, A. Artemenko, J. Kousal, D. Slavínská, A. Choukourov, and H. Biederman. Nylon-sputtered nanoparticles: fabrication and basic properties. *Journal of Physics D: Applied Physics*, 45(49):495301, nov 2012.

[10] M. Drábik, A. Serov, O. Kylián, A. Choukourov, A. Artemenko, J. Kousal, O. Polonskyi, and H. Biederman. Deposition of fluorocarbon nanoclusters by gas aggregation cluster source. *Plasma Processes and Polymers*, 9(4):390–397, feb 2012.

[11] P. Solař, O. Polonskyi, A. Olbricht, A. Hinz, A. Shelemin, O. Kylián, A. Choukourov, F. Faupel, and H. Biederman. Single-step generation of metal-plasma polymer multicore@shell nanoparticles from the gas phase. *Scientific Reports*, 7(1), aug 2017.

[12] O. Kylián, A. Kuzminova, M. Vaydulych, M. Cieslar, I. Khalakhan, J. Hanuš, A. Choukourov, D. Slavínská, and H. Biederman. Core@shell cu/hydrocarbon plasma polymer nanoparticles prepared by gas aggregation cluster source followed by in-flight plasma polymer coating. *Plasma Processes and Polymers*, 15(1):1700109, aug 2017.

[13] Y. Huttel, editor. *Gas-Phase Synthesis of Nanoparticles*. Wiley VCH Verlag GmbH, 2017.

[14] H. Haberland, M. Karrais, and M. Mall. A new type of cluster and cluster ion source. *Zeitschrift fuer Physik D Atoms, Molecules and Clusters*, 20(1-4):413–415, mar 1991.

[15] H. Haberland, M. Karrais, M. Mall, and Y. Thurner. Thin films from energetic cluster impact: A feasibility study. *Journal of Vacuum Science & Technology A: Vacuum, Surfaces, and Films*, 10(5):3266–3271, sep 1992.

[16] H. Haberland, M. Mall, M. Moseler, Y. Qiang, T. Reiners, and Y. Thurner. Filling of micron-sized contact holes with copper by energetic cluster impact. *Journal of Vacuum Science & Technology A: Vacuum, Surfaces, and Films*, 12(5):2925–2930, sep 1994.

[17] C. Binns. Nanoclusters deposited on surfaces. *Surface Science Reports*, 44(1-2):1–49, oct 2001.

[18] C. Binns. Chapter 3 production of nanoparticles on supports using gas-phase deposition and MBE. In *Metallic Nanoparticles*, pages 49–71. Elsevier, 2008.

[19] K. Wegner, P. Piseri, H. Vahedi Tafreshi, and P. Milani. Cluster beam deposition: a tool for nanoscale science and technology. *Journal of Physics D: Applied Physics*, 39(22):R439–R459, nov 2006.

[20] J. Kratochvíl, A. Kuzminova, O. Kylián, and H. Biederman. Comparison of magnetron sputtering and gas aggregation nanoparticle source used for fabrication of silver nanoparticle films. *Surface and Coatings Technology*, 275:296–302, aug 2015.

[21] M. Goto, J. Murakami, Y. Tai, K. Yoshimura, K. Igarashi, and S. Tanemura. Formation of alumina fine particles by a magnetron sputtering - gas aggregation method. *Zeitschrift fuer Physik D Atoms, Molecules and Clusters*, 40(1-4):115–118, may 1997.

[22] R. M. Nielsen, S. Murphy, C. Strebel, M. Johansson, I. Chorkendorff, and J. H. Nielsen. The morphology of mass selected ruthenium nanoparticles from a magnetron-sputter gas-aggregation source. *Journal of Nanoparticle Research*, 12(4):1249–1262, dec 2009.

[23] A.N. Banerjee, R. Krishna, and B. Das. Size controlled deposition of cu and si nano-clusters by an ultra-high vacuum sputtering gas aggregation technique. *Applied Physics A*, 90(2):299–303, sep 2007.

[24] T. Acsente, R. F. Negrea, L. C. Nistor, C. Logofatu, E. Matei, R. Birjega, C. Grisolia, and G. Dinescu. Synthesis of flower-like tungsten nanoparticles by magnetron sputtering combined with gas aggregation. *The European Physical Journal D*, 69(6), jun 2015.

[25] A. Marek, J. Valter, S. Kadlec, and J. Vyskočil. Gas aggregation nanocluster source — reactive sputter deposition of copper and titanium nanoclusters. *Surface and Coatings Technology*, 205:S573–S576, jul 2011.

[26] R. Morel, A. Brenac, P. Bayle-Guillemaud, C. Portemont, and F. La Rizza. Growth and properties of cobalt clusters made by sputtering gas-aggregation. *The European Physical Journal D - Atomic, Molecular and Optical Physics*, 24(1-3):287–290, jun 2003.

[27] Y. Qiang, J. Antony, A. Sharma, J. Nutting, D. Sikes, and D. Meyer. Iron/iron oxide core-shell nanoclusters for biomedical applications. *Journal of Nanoparticle Research*, 8(3-4):489–496, oct 2005.

[28] L. Martínez, M. Díaz, E. Román, M. Ruano, D. Llamosa P., and Y. Huttel. Generation of nanoparticles with adjustable size and controlled stoichiometry: Recent advances. *Langmuir*, 28(30):11241–11249, jul 2012.

[29] Y. H. Xu, J. Bai, and J.-P. Wang. High-magnetic-moment multifunctional nanoparticles for nanomedicine applications. *Journal of Magnetism and Magnetic Materials*, 311(1):131–134, apr 2007.

[30] Y.-H. Xu and J.-P. Wang. Magnetic properties of heterostructured co–au nanoparticles direct-synthesized from gas phase. *IEEE Transactions on Magnetics*, 43(6):3109–3111, jun 2007.

[31] J. Hanuš, M. Vaidulych, O. Kylián, A. Choukourov, J. Kousal, I. Khalakhan, M. Cieslar, P. Solař, and H. Biederman. Fabrication of ni@ti core–shell nanoparticles by modified gas aggregation source. *Journal of Physics D: Applied Physics*, 50(47):475307, nov 2017.

[32] T. Kretková, J. Hanuš, O. Kylián, P. Solař, M. Dopita, M. Cieslar, I. Khalakhan, A. Choukourov, and H. Biederman. In-flight modification of ni nanoparticles by tubular magnetron sputtering. *Journal of Physics D: Applied Physics*, 52(20):205302, mar 2019.

[33] H. Yasuda. *Plasma Polymerization*. Academic Press, 1985.

[34] B. Akhavan, K. Jarvis, and P. Majewski. Hydrophobic plasma polymer coated silica particles for petroleum hydrocarbon removal. *ACS Applied Materials & Interfaces*, 5(17):8563–8571, aug 2013.

[35] N. Inagaki. *Plasma Surface Modification and Plasma Polymerization*. Taylor & Francis Inc, 1996.

[36] I. Muzammil, Y. Li, and M. Lei. Tunable wettability and pH-responsiveness of plasma copolymers of acrylic acid and octafluorocyclobutane. *Plasma Processes and Polymers*, 14(10):1700053, jul 2017.

[37] M. Drábik, O. Polonskyi, O. Kylián, J. Čechvala, A. Artemenko, I. Gordeev, A. Choukourov, D. Slavínská, I. Matolínová, and H. Biederman. Super-hydrophobic coatings prepared by RF magnetron sputtering of PTFE. *Plasma Processes and Polymers*, 7(7):544–551, jun 2010.

[38] Z. Zhang, W. Knoll, and R. Förch. Amino-functionalized plasma polymer films for DNA immobilization and hybridization. *Surface and Coatings Technology*, 200(1-4):993–995, oct 2005.

[39] A. A. Meyer-Plath, K. Schröder, B. Finke, and A. Ohl. Current trends in biomaterial surface functionalization—nitrogen-containing plasma assisted processes with enhanced selectivity. *Vacuum*, 71(3):391–406, may 2003.

[40] C. Vreuls, G. Zocchi, B. Thierry, G. Garitte, S. S. Griesser, C. Archambeau, C. Van de Weerdt, J. Martial, and H. Griesser. Prevention of bacterial biofilms by covalent immobilization of peptides onto plasma polymer functionalized substrates. *Journal of Materials Chemistry*, 20(37):8092, 2010.

[41] H. Biederman and Y. Osada. *Plasma Polymerization Processes (Plasma Technology)*. Elsevier Science, 1992.

[42] H. Biederman. *Plasma Polymer Films*. Imperial College Press, 2004.

[43] H. Biederman. RF sputtering of hydrocarbon polymers and their derivatives. *Surface and Coatings Technology*, 174-175:27–32, oct 2003.

[44] I. Kholodkov. Plasma polymers prepared by RF sputtering of polyethylene. *Vacuum*, 70(4):505–509, apr 2003.

[45] A. Choukourov, J. Hanuš, J. Kousal, A. Grinevich, Y. Pihosh, D. Slavínská, and H. Biederman. Plasma polymer films from sputtered polyimide. *Vacuum*, 81(4):517–526, nov 2006.

[46] O. Kylián, J. Hanuš, A. Choukourov, J. Kousal, D. Slavínská, and H. Biederman. Deposition of amino-rich thin films by RF magnetron sputtering of nylon. *Journal of Physics D: Applied Physics*, 42(14):142001, jun 2009.

[47] D. D. Neiswender. The polymerization of benzene in a radiofrequency discharge. In *Advances in Chemistry*, pages 338–349. AMERICAN CHEMICAL SOCIETY, jun 1969.

[48] A.R. Denaro, P.A. Owens, and A. Crawshaw. Glow discharge polymerization—styrene. *European Polymer Journal*, 4(1):93–106, feb 1968.

[49] L. F. Thompson and G. Smolinsky. A scanning electron microscope study of plasma-polymerized organosilicon films suitable for use as lightguides. a determination of the cause of signal attenuation. *Journal of Applied Polymer Science*, 16(5):1179–1190, may 1972.

[50] A. Melzer. *Physics of Dusty Plasmas*. Springer International Publishing, 2019.

[51] A. Serov. *Preparation and basic properties of nanostructured plasma polymers*. PhD thesis, Charles University, 2014.

[52] A. Shelemin, D. Nikitin, A. Choukourov, O. Kylián, J. Kousal, I. Khalakhan, I. Melnichuk, D. Slavínská, and H. Biederman. Preparation of biomimetic nano-structured films with multi-scale roughness. *Journal of Physics D: Applied Physics*, 49(25):254001, may 2016.

[53] P. Hlídek, J. Hanuš, H. Biederman, D. Slavínská, and J. Pešička. Composite ag/c:h:n films prepared by planar magnetron deposition. *Thin Solid Films*, 516(14):4581–4586, may 2008.

[54] J. Hanus, M. Drabik, P. Hlidek, H. Biederman, G. Radnoczi, and D. Slavinska. Some remarks on ag/c:h nanocomposite films. *Vacuum*, 83(2):454–456, sep 2008.

[55] O. Polonskyi, P. Solař, O. Kylián, M. Drábik, A. Artemenko, J. Kousal, J. Hanuš, J. Pešička, I. Matolínová, E. Kolíbalová, D. Slavínská, and H. Biederman. Nanocomposite metal/plasma polymer films prepared by means of gas aggregation cluster source. *Thin Solid Films*, 520(12):4155–4162, apr 2012.

[56] P. Solař, O. Kylián, O. Polonskyi, A. Artemenko, D. Arzhakov, M. Drábik, D. Slavínská, M. Vandrovcová, L. Bačáková, and H. Biederman. Nanocomposite coatings of ti/c:h plasma polymer particles providing a surface with variable nanoroughness. *Surface and Coatings Technology*, 206(21):4335–4342, jun 2012.

[57] O. Kylián, O. Polonskyi, J. Kratochvíl, A. Artemenko, A. Choukourov, M. Drábik, P. Solař, D. Slavínská, and H. Biederman. Control of wettability of plasma polymers by application of ti nano-clusters. *Plasma Processes and Polymers*, 9(2):180–187, oct 2011.

[58] O. Kylián, J. Kratochvíl, J. Hanuš, O. Polonskyi, P. Solař, and H. Biederman. Fabrication of cu nanoclusters and their use for production of cu/plasma polymer nanocomposite thin films. *Thin Solid Films*, 550:46–52, jan 2014.

[59] M. Vaidulych, J. Hanuš, T. Steinhartová, O. Kylián, A. Choukourov, J. Beranová, I. Khalakhan, and H. Biederman. Deposition of ag/a-c:h nanocomposite films with ag surface enrichment. *Plasma Processes and Polymers*, 14(11):1600256, jun 2017.

[60] A. Choukourov, O. Kylián, M. Petr, M. Vaidulych, D. Nikitin, J. Hanuš, A. Artemenko, A. Shelemin, I. Gordeev, Z. Kolská, P. Solař, I. Khalakhan, A. Ryabov, J. Májek, D. Slavínská, and H. Biederman. RMS roughness-independent tuning of surface wettability by tailoring silver nanoparticles with a fluorocarbon plasma polymer. *Nanoscale*, 9(7):2616–2625, 2017.

[61] O. Kylián, A. Shelemin, P. Solař, P. Pleskunov, D. Nikitin, A. Kuzminova, R. Štefaníková, P. Kúš, M. Cieslar, J. Hanuš, A. Choukourov, and H. Biederman. Magnetron sputtering of polymeric targets: From thin films to

heterogeneous metal/plasma polymer nanoparticles. *Materials*, 12(15):2366, jul 2019.

[62] C. Cassidy, V. Singh, P. Grammatikopoulos, F. Djurabekova, K. Nordlund, and M. Sowwan. Inoculation of silicon nanoparticles with silver atoms. *Scientific Reports*, 3(1), oct 2013.

[63] M. Ohring. *The Materials Science of Thin Films.* ACADEMIC PR INC, 1991.

[64] G. Sauerbrey. Verwendung von schwingquarzen zur waegung duenner schichten und zur mikrowaegung. *Zeitschrift fuer Physik*, 155(2):206–222, apr 1959.

[65] R. K. Marcus and J. A. C. Broekaert, editors. *Glow Discharge Plasmas in Analytical Spectroscopy.* WILEY, 2003.

[66] M. Mishchenko, L. D. Travis, and A. Lacis. *Multiple Scattering of Light by Particles.* Cambridge University Press, 2013.

[67] E. E. Miteva. Synthese von nanokompositmaterialien in einer kombinierten hf-entladung mit gas-aggregationsquelle. Master's thesis, Christian-Albrechts-Universität zu Kiel, 2020.

[68] S. N. Pandis J. H. Seinfeld. *Atmospheric Chemistry and Physics: From Air Pollution to Climate Change.* WILEY, 2016.

[69] R. Beanland P. J. Goodhew, J. Humphreys. *Electron Microscopy and Analysis.* Taylor & Francis Ltd, 2000.

[70] D. A. Skoog, S. R. Crouch, and Holler F. J. *Principles of Instrumental Analysis.* BROOKS COLE PUB CO, 2017.

[71] K. L. Kelly, E. Coronado, L. L. Zhao, and G. C. Schatz. The optical properties of metal nanoparticles: the influence of size, shape, and dielectric environment. *The Journal of Physical Chemistry B*, 107(3):668–677, jan 2003.

[72] V. Garofano, L. Stafford, B. Despax, R. Clergereaux, and K. Makasheva. Cyclic evolution of the electron temperature and density in dusty low-pressure radio frequency plasmas with pulsed injection of hexamethyldisiloxane. *Applied Physics Letters*, 107(18):183104, nov 2015.

[73] L. Boufendi, M. Ch. Jouanny, E. Kovacevic, J. Berndt, and M. Mikikian. Dusty plasma for nanotechnology. *Journal of Physics D: Applied Physics*, 44(17):174035, apr 2011.

[74] J. Berndt, E. Kovacevic, I. Stefanovic, O. Stepanovic, S. H. Hong, L. Boufendi, and J. Winter. Some aspects of reactive complex plasmas. *Contributions to Plasma Physics*, 49(3):107–133, apr 2009.

[75] J. Kousal, J. Hanuš, A. Choukourov, O. Polonskyi, H. Biederman, and D. Slavínská. In situ diagnostics of RF magnetron sputtering of nylon. *Plasma Processes and Polymers*, 6(S1):S803–S807, may 2009.

[76] A. Choukourov, P. Pleskunov, D. Nikitin, V. Titov, A. Shelemin, M. Vaidulych, A. Kuzminova, P. Solař, J. Hanuš, J. Kousal, O. Kylián, D. Slavínská, and H. Biederman. Advances and challenges in the field of plasma polymer nanoparticles. *Beilstein Journal of Nanotechnology*, 8:2002–2014, sep 2017.

[77] A. Shelemin, P. Pleskunov, J. Kousal, J. Drewes, J. Hanuš, S. Ali-Ogly, D. Nikitin, P. Solař, J. Kratochvíl, M. Vaidulych, M. Schwartzkopf, O. Kylián, O. Polonskyi, T. Strunskus, F. Faupel, S. V. Roth, H. Biederman, and A. Choukourov. Nucleation and growth of magnetron-sputtered ag nanoparticles as witnessed by time-resolved small angle x-ray scattering. *Particle & Particle Systems Characterization*, 37(2):1900436, dec 2019.

[78] O. Kylián, A. Kuzminova, R. Štefaníková, J. Hanuš, P. Solař, P. Kúš, M. Cieslar, A. Choukourov, and H. Biederman. Silver/plasma polymer strawberry-like nanoparticles produced by gas-phase synthesis. *Materials Letters*, 253:238–241, oct 2019.

[79] O. Kylián, R. Štefaníková, A. Kuzminova, J. Hanuš, P. Solař, P. Kúš, M. Cieslar, and H. Biederman. In-flight plasma modification of nanoparticles produced by means of gas aggregation sources as an effective route for the synthesis of core-satellite ag/plasma polymer nanoparticles. *Plasma Physics and Controlled Fusion*, 62(1):014005, oct 2019.

List of Figures

List of Tables

List of Abbreviations

C:H or C:H:N or C:H:N:O – elemental composition of plasma polymer
CNT – classical nucleation theory
DC – direct current
GAS – gas aggregation source
HIPIMS – high-power impulse magnetron sputtering
HMDSO – hexamethyldisiloxane
LSPR – localized surface plasmon resonance
NPs – nanoparticles
OES – optical emission spectroscopy
PTFE – polytetrafluoroethylene
QCM – quartz crystal microbalance
RF – radio frequency
SEM – scanning electron microscopy
TEM – transmission electron microscopy
UV-Vis – ultraviolet-visible spectrometry
XPS – X-ray photoelectron spectroscopy